Research Square

Preprints are preliminary reports that have not undergone peer review.
They should not be considered conclusive, used to inform clinical practice,
or referenced by the media as validated information.

Early Reelin Loss Disrupts Lamination in the pallial cortex including Taenia Tecta, and Indusium Griseum

Erica Lucia Crapanzano
University of Pisa
Melissa Barber
University College London
Eleonora Sara Bacci
University of Pisa
Chiara Gabellini
University of Pisa
José Luis Ferran
Biomedical Research Institute of Murcia Pascual Parrilla–IMIB
Ugo Borello
ugo.borello@unipi.it

University of Pisa

Research Article

Keywords:

Posted Date: October 22nd, 2026

DOI: https://doi.org/10.21203/rs.3.rs-11141909/v1

License: This work is licensed under a Creative Commons Attribution 4.0 International License.
Read Full License

Additional Declarations: No competing interests reported.

Early Reelin Loss Disrupts Lamination in the pallial cortex including Taenia Tecta, and Indusium Griseum

Erica Lucia Crapanzano[1]*, Melissa Barber[2], Eleonora Sara Bacci[1], Chiara Gabellini[1], José Luis Ferran[3,4], Ugo Borello[1]*

[1.]Unit of Cell and Developmental Biology, Department of Biology, University of Pisa, Italy

[2.]Dementia Research Institute, University College London, London, UK

[3.]Biomedical Research Institute of Murcia Pascual Parrilla–IMIB, 30120 Murcia, Spain

[4.]Department of Human Anatomy and Psychobiology, Faculty of Medicine, University of Murcia, Murcia E30100, Spain

*To whom correspondence should be addressed: erica.crapanzano@phd.unipi.it, ugo.borello@unipi.it

Abstract

The secreted extracellular glycoprotein reelin (RELN) is essential for mammalian corticogenesis, yet its spatio-temporal requirements across pallial subdivisions remain incompletely understood. Here, we validate a conditional knockout mouse model targeting *Reln* exon 3 to dissect the role of reelin during early pallial development. By crossing floxed *Reln* mice with pan-telencephalic (*Foxg1-Cre*) or pallium-restricted (*Emx1-Cre*) drivers, we investigated the effects of broad early deletion (E9.5) against delayed, domain-restricted ablation (E10.5). At stage E12.5 Cajal–Retzius (CR) cell generation, and spatial distribution remained intact, confirming that downstream phenotypes stem directly from the loss of extracellular signaling. Pan-telencephalic deletion using *Foxg1Cre* disrupted the cortical plate–intermediate zone boundary at E14.5 and caused a severe inversion of neocortical lamination, alongside piriform cortex dysgenesis, from embryonic stages into mature adulthood (P30). We identified an undescribed vulnerability in the taenia tecta (TT) and indusium griseum (IG), limbic allocortical territories rostral to the hippocampus proper. Furthermore, mapping of the nuclear receptor *Nr4a2* revealed defective nuclear condensation within the claustrum proper and dorsal endopiriform nucleus, accompanied by the ectopic invasion of claustral cells into the insular cortex and the loss of subplate organization. In contrast, adult $Reln^{fl/fl};Emx1^{Cre/+}$ brains retained normal stratification and allocortical structure, demonstrating substantial compensation by spared subpallial interneurons and non-

pallial CR lineages. Collectively, these findings establish reelin as a universal regulator of pallial morphogenesis, orchestrating allocortical lamination and non-laminar nuclear assembly far beyond its canonical role in neocortical inside-out stratification.

Keywords:
Cajal-Retzius cells, allocortex, isocortex, mesocortex, forebrain, telencephalon

Abbreviations
A: Amygdala
ac: Anterior commissure
CA1: Cornu ammonis 1
CA2: Cornu ammonis 2
CA3: Cornu ammonis 3
Cb: Cerebellum
cc: Corpus callosum
Clp: Claustrum proper
CP: Cortical plate
Cx: Cortex
D: Dorsal pallium
DG: Dentate gyrus
Di: Diencephalon
DL: Dorsal lateral pallium
DM: Dorsal medial pallium
E: Eye
ECx: entorhinal cortex
EpD: Endopiriform nucleus (dorsal)
fx: Fornix
Hb: Habenula
hc: Hippocampal commissure
Hi: Hippocampus
IG: Indusium griseum
IL: Infralimbic cortex
Ins: Insular cortex
IZ: Intermediate zone
L: Lateral pallium
LV: Lateral ventricle
M: Medial pallium
MB: Midbrain

MZ: Marginal zone
Pal: Pallidum
PalSe: Pallial Septum
pc: Posterior commissure
PG: Pineal gland
Pir: Piriform cortex
PP: Preplate
PT: Pretectum
PTh: Prethalamus
PThE: Prethalamic eminence
rf: rhinal fissure
Rh: Rhombencephalon
SCS: Subcallosal sling
Se: Septum
Sp: Subplate
SS: Somatosensory cortex
St: Striatum
Sub: Subiculum
T: Telencephalon
Th: Thalamus
TT: Taenia tecta
TTd: Dorsal taenia tecta
TTv: Ventral taenia tecta
VC: Ventricular cavity
VZ: Ventricular zone
WM: White matter

Introduction

The mammalian telencephalon is established through an early, evolutionarily conserved regionalization process that segregates the embryonic alar plate into distinct subpallial and pallial territories, yielding structures shared across mammalian species (Lucero-Arteaga et al., 2025; Lucero-Arteaga et al., 2026; Puelles & Rubenstein, 2003, 2015). Within the framework of the prosomeric model and its pallial partition scheme, the pallium is divided into four primary progenitor domains - medial, dorsal, lateral, and ventral - which give rise, respectively, to the hippocampal formation, isocortex (neocortex), claustral/insular complex, and piriform cortex (Puelles, 2017; Puelles & Rubenstein, 2003). Complementarily, the cortical ring model conceptualizes pallial development

through definition of concentric rings, progressing from peripheral allocortical territories through mesocortical zones to central isocortical regions (García-Cabezas et al., 2023; Puelles & García-calero, 2024; Sanides, 1962). The specification across these pallial domains is driven by an upstream hierarchy of transcription factors that exhibit distinct spatio-temporal expression patterns (Puelles et al., 2000).

During mammalian pallial development, neurogenesis progresses to form predominantly laminated structures. In cortical regions, this process begins with the formation of the preplate (PP), a transient structure composed of early-generated neurons superficial to the ventricular zone (VZ). As asymmetric divisions of cortical progenitor cells drive neurogenesis forward, newly generated neurons migrate into the PP, splitting it into two distinct compartments: the superficial marginal zone (MZ), enriched in Cajal-Retzius (CR) cells, and the deeper subplate (Sp) (Franco & Müller, 2013; Götz & Huttner, 2005). The cortical plate (CP) subsequently emerges between the MZ and Sp, expanding through the continuous addition of neurons. This accretion follows the classic "inside-out" lamination pattern, wherein early-born neurons settle in deep layers while later-born neurons migrate past them to occupy progressively superficial positions (Angevine & Sidman, 1961; Cadwell et al., 2019).

At the molecular level, while early signaling networks provide neural progenitors with positional information, the extracellular matrix glycoprotein reelin (RELN) plays a critical role in regulating neuronal migration and cortical assembly (Gil et al., 2014; Martínez-Cerdeño & Noctor, 2014; E. Soriano & Del Rio, 2005). By orchestrating preplate splitting and "*inside-out*" radial migration, reelin signaling ensures that newborn neurons migrate past earlier-born cohorts to establish stratified cortical layers (Caviness, 1982; D'Arcangelo et al., 1995). reelin has been hypothesized to act either as a chemoattractant guiding neurons to their definitive destinations or as a stop signal terminating migration (Dulabon et al., 2000; Gilmore & Herrup, 2000; Jossin, 2004). During early embryogenesis, telencephalic reelin is primarily secreted by two distinct lineages: subpallial GABAergic interneurons migrating tangentially into the cortex, and glutamatergic CR cells residing in the superficial marginal zone. These CR cells originate from four distinct embryonic niches: the ventral pallium, cortical hem, pallial septum, and diencephalic prethalamic eminence (Barber & Pierani, 2016; Bielle et al., 2005; Causeret et al., 2021; Elorriaga et al., 2023; Ruiz-Reig & Studer, 2017; Vilchez-Acosta et al., 2022). Historically, the developmental role of reelin was characterized using the spontaneous *reeler* mutant mouse (Arcangelo & Curran, 1998; D'Arcangelo et al., 1995), establishing reelin as a cornerstone of *inside-out* cortical lamination (Jossin et al., 2003; Katsuyama & Terashima, 2009; Mingo-moreno et al., 2024). More recently, lineage-specific deletions (*Calb2-Cre* for CR cells; *Gad2-Cre* for interneurons) demonstrated that CR-derived reelin drives inside-out layer positioning. Conversely, interneuron-derived reelin prevents premature neuronal invasion of layer I, refines final neuronal positioning, and contributes to hippocampal morphogenesis (Pahle et al., 2019; Vilchez-Acosta et al., 2022). To study

how spatio-temporal variations in early reelin ablation affect pallial development, we took advantage of a novel conditional knockout (*reelin* cKO) mouse line carrying floxed *Reln* exon 3, generated via homologous recombination. We validated this conditional line and crossed *Reln*$^{fl/fl}$ mice with either the pan-telencephalic *Foxg1-Cre* driver or the pallium-restricted *Emx1-Cre* driver to generate distinct conditional ablation patterns. The forkhead factor *Foxg1* acts as a master regulator of early pan-telencephalic identity, expressed broadly across pallial and subpallial territories starting at embryonic day 8.5-9 (E8.5-E9) (Xuan et al., 1995). In contrast, the homeobox gene *Emx1* displays a delayed (~E10.5), domain-restricted profile along a mediolateral gradient covering the medial, dorsal, and lateral pallium—while sparing the ventral pallium and subpallium (Gulisano et al., 1996; Simeone et al., 1992). Harnessing these divergent expression profiles through *Foxg1-Cre* and *Emx1-Cre* driver lines enables a systematic comparison of developmental signaling across broad pan-telencephalic versus domain-restricted pallial territories (Gorski et al., 2002; Hébert & McConnell, 2000; Magno et al., 2022). Our findings confirm an essential early role for reelin in corticogenesis and identify it as an early regulator of anterior medial pallial structures, specifically the taenia tecta (TT) and indusium griseum (IG). These regions, representing a rostral extension of the Ammonic region within the limbic system (Di Ieva et al., 2015) have not been previously studied in the frame of a reelin conditional ablation paradigm. Ultimately, this comparative cKO strategy demonstrates that reelin plays a pivotal role during the early stages of pallial derivative patterning and in the structural organization of postmitotic neurons.

Material and Methods

The conditional *Reln* mouse strain used for this research project was generated from C57BL/6N-Atm1Brd mouse ES cell clones (DEPD00533_5_A03 and DEPD00533_5_F01), obtained from the Mouse Biology Program (https://mbp.mousebiology.org) and made into Relntm1a(KOMP)Mbp ES cells using the KOMP Repository (https://www.komp.org/redirect.html) at the University of California Davis (U42RR024244): Mouse (Relntmla(KOMP)/C57b/6) [komp #120606]; project ID: CSD25412; Design ID: 49754. A promoter driven cassette was used to generate the 'Knockout-first allele' that targeted a exon 3 (22937-22970) of *Reln* Chr5:21884454-22344702 bp, common to all transcript variants that, when deleted, creates a frame-shift mutation.

Long-range PCR at either the 5’ or 3’ end of the vector was carried out to confirm correct KOMP CSD targeted alleles and the presence of the 3’ LoxP site confirmed using quantitative Taqman PCR at UCKOMP Davis. Mouse ES clones (DEPD00533_5_A03

and DEPD00533_5_F01) with >50% euploidy cells were microinjected into blastocysts of Agouti female mice at ICH UCL Transgenic mouse service, with two chimeric founder male mice derived from the DEPD00533_5_F01 and DEPD00533_5_A03 clones taken forward in matings and back-crossed with C57Bl/6N mice for five generations to outbreed the Agouti genetic background. Conditional *Reln*$^{fl/+}$ mice were obtained by their mating with *Rosa26FLPe* knock-in mice (B6.129S4-Gt(ROSA)26Sortm1(FLP1)Dym/RainJ) - JAX stock #009086 (Farley et al., 2000)) to remove the flippase recognition (Frt) sites, *LacZ* and *Neo* cassettes. The remaining loxP sites flank *Reln* exon 3. *Reln*$^{fl/+}$ mice were subsequently mated with *FoxG1Cre (*B6.129P2(Cg)-Foxg1tm1(cre)Skm/J - JAX stock #006084 - (Hébert & McConnell, 2000), hereafter referred to as *Foxg1*$^{Cre/+}$*)* or *Emx1Cre* mice (B6.129S2-Emx1tm1(cre)Krj/J - JAX stock #005628 - (Kessaris et al., 2006)).
For all conditional KO models, mutant embryos were defined as homozygous for the floxed allele and positive for the specific Cre driver (i.e., *Reln*$^{fl/fl}$ *;Foxg1*$^{Cre/+}$ or *Reln*$^{fl/fl}$ *;Emx1*$^{Cre/+}$). To ensure rigorous comparisons, heterozygous littermates positive for the respective Cre driver (i.e., *Reln*$^{fl/+}$ *;Foxg1*$^{Cre/+}$or *Reln*$^{fl/fl}$ *;Emx1*$^{Cre/+}$) were strictly utilized as controls.
To study CRE activity a reporter mouse was used (B6.129X1-Gt(ROSA)26Sortm1(EYFP)Cos/J - JAX stock #006148 (Srinivas et al., 2001)), hereafter referred to as *R26R-YFP.*
Both the male and female postnatal and adult forebrains were used in this study.
Mice were maintained under a 12 h light/12 h dark cycle, at constant temperature and humidity, with food and water provided *ad libitum*. All experimental procedures were performed in accordance with the UK Animals (Scientific Procedures) Act 1986 and the UCL institutional guidelines under Prof. Parnavelas PPL 70/8227, and in accordance with the European Union Communities Council Directive (2010/63/EU) and Italian laws (D.L.26/2014). Protocols were approved by the Italian Council on Animal Care in accordance with the Italian law (Italian Government authorizations AC179.N.SRF and AC179.N.KHR).

Mouse sample collection and genotyping

Mouse embryos were collected at embryonic stage E12.5, E14.5, E18.5, considering as E0.5 on the morning when the vaginal plug is present. For E12.5 and E14.5 stages, entire heads were isolated, whereas at E18.5 only the brains were dissected. Instead, postnatal brains were collected at postnatal day 30 (P30) via microdissection. All samples were fixed in 4% paraformaldehyde (PFA) at 4°C either for 1.5 h or overnight, depending on the experiment. Caudal tissue from each embryo was collected in parallel for genomic DNA extraction.
For genotyping embryonic tail tissue was digested overnight at 55°C in lysis buffer (1M Tris-HCl pH 8, 0.5 M EDTA pH 8, 5 M NaCl, 0.5% SDS, 0.5 mg/ml proteinase K). Samples

were centrifuged for 10 minutes at 17,000 × g, and the supernatant was precipitated with 1 ml of 96% ethanol. After centrifugation, the DNA pellet was washed with 70% ethanol and resuspended in water. Genotyping was performed using polymerase chain reaction (PCR) protocols, with specific conditions for each mouse CRE lines, as described (Hébert & McConnell, 2000; Kessaris et al., 2006). Regarding the *Reln* line genotyping, we used the following primers to discriminate wild-type from floxed allele: FW: CTTAGACCCACTCTGTCCTCACACC, RW: GGAGACCACACAACACAGTAGACTGG, producing amplicon of 290 bp in the case of wild-type allele and 431 bp for $Reln^{fl}$ allele.

Tissue preparation and cryosectioning

Following fixation, brains were washed three times in PBS and cryoprotected overnight at 4°C in a 30% sucrose/PBS solution. Tissues were embedded in OCT (Tissue-Tek), rapidly frozen, and stored at -80°C. We cut 20 µm coronal cryosections and collected them on SuperFrost Plus slides (Epredia) and stored them at -80°C.

Probe synthesis and *In Situ* Hybridization (ISH)

Total RNA was extracted, reverse-transcribed into cDNA, and amplified using gene-specific primers. Purified amplicons, using the QIAquick Gel Extraction Kit (QIAGEN), were cloned into the TOPO TA Cloning vector (Invitrogen) and transformed into DH5α E. coli (Thermo Fisher). Insert sequence and orientation were validated by Sanger sequencing. Antisense RNA probes were synthesized in vitro using a DIG RNA Labeling Kit (Roche) and purified with the RNeasy Mini Kit (QIAGEN).
Primer sequences and target regions utilized for probe synthesis included: *reelin* (from 372.490 nt to 372724 nt - NC_000071); *Lpl* (FW: CCAAGCTGGTGGGAAATG, RW:GTCAGGCCAGCTGAAGTA), *Peg10* (FW: CAAGTGAAAAGAGGGTGGAAAC, RW:ACTTCCTTTTCAAGCTGAGGTG), *Zbtb20* (FW:GTGCACTCGCATCGTGTC , RW:GTGAAGAGGGCTGGCAGA); *Lmo3* (FW: CTGAATAGGGTAGCGGTAGGTG; RW: GAAGTTGTTCACATGCTACCCA); *Nr4a2* (FW: GACAGCAGTCCTCCATTAAGGT, RW:TCATCTGATAGTCAGGGTTTGC); *Slit2* (Kind gift from Thomas Theil, Edinburgh).
For the ISH procedure, cryosections were post-fixed in 4% PFA for 15 minutes at 4°C and permeabilized with proteinase K (1 µg/ml). Digestion times were developmentally adjusted (5 minutes at RT for E12.5 and E14.5; 10 minutes for E18.5). Following acetylation and permeabilization in 0,1% Triton X-100, sections were pre-hybridized for 2 hours at RT, with hybridization buffer (50% formamide, 5X SSC, yeast tRNA, salmon sperm DNA, Denhardt's solution, H_2O). Hybridization was carried out by applying an RNA antisense probe (200–400 ng/ml) diluted in hybridization buffer, previously denatured at 72°C, followed by overnight incubation at 65°C in a humidified chamber. Post-hybridization sections were washed in 5X SSC and subsequently subjected to high-stringency washes in 0.2X SSC at 65°C. Probe detection was achieved using an alkaline

phosphatase-conjugated anti-DIG antibody (1:5000, Roche) and NBT/BCIP colorimetric substrate. Sections were mounted in Eukitt Klassic after overnight air-drying.

Nissl staining and immunofluorescence

For Nissl staining, slides were washed in PBS and stained with 0,04% toluidine blue for 10, 15, or 40 minutes, respectively for E14.5, E18.5 and P30. Tissues were dehydrated through a graded ethanol series, cleared in xylene, and mounted with Eukitt Klassic.
For immunofluorescence, sections were rehydrated, permeabilized in 0,1% Triton X-100 (PBT), and blocked in 10% donkey serum for 1 hour at RT. Primary antibodies were applied overnight at 4°C in 3% donkey serum. Sections were subsequently incubated with fluorophore-conjugated secondary antibodies and Hoechst nuclear stain (1:1000) for 4 hours at RT. reelin immunostaining required prior antigen retrieval using boiling 10 mM sodium citrate buffer pH 6 with 0.05% Triton X-100 for 15 minutes. Slides were mounted using Fluoromount (Sigma-Aldrich). The primary antibodies used are guinea pig anti-Tbr1 (1:400; Synaptic Systems, Cat. No. 328 005), rabbit anti-Mef2c (1:250; Abcam, Cat. No. ab319010), goat anti-TRP73 (1:50; Santa Cruz Biotechnology, Cat. No. sc-9651), rat anti-Ctip2 (1:500; Abcam, Cat. No. ab18465), rabbit anti-Tbr2 (1:100; Abcam, Cat. No. ab216870), rabbit anti-CALB2 (1:1000; Sigma-Aldrich, Cat. No. C7479), and mouse anti-reelin (1:200; Millipore, Cat. No. MAB5366). Instead, the secondary antibodies used are all diluted at 1:500: donkey anti-rabbit IgG conjugated to Cy3 (Jackson ImmunoResearch), donkey anti-mouse IgG conjugated to Cy2 (Jackson ImmunoResearch), goat anti-rat IgG conjugated to Alexa Fluor 555 (Abcam), goat anti-guinea pig IgG conjugated to FITC (Sigma-Aldrich), donkey anti-guinea pig IgG conjugated to Alexa Fluor 555 (Sigma-Aldrich), and donkey anti-goat IgG conjugated to Cy2 (Jackson ImmunoResearch).

Quantitative image analysis

Image acquisition

Images were acquired using multiple microscopy platforms depending on sample type and imaging requirements. Whole-mount samples were acquired using stereomicroscope Nikon SMZ1500. Images in bright-field of *in situ* hybridization (ISH) and Nissl-stained samples were performed by Nikon Eclipse Ti microscope. High-resolution fluorescence images were acquired using Nikon Confocal Microscope AX. Confocal imaging was employed for all immunofluorescence experiments to obtain optical sections and detailed cellular and subcellular localization of fluorescent signals. Objectives with magnifications of 20x, 40x, or 60x were selected according to the size of the samples and the level of detail required.

Quantitative laminar analysis

Confocal images were processed in Fiji to assess the cortical distribution of $TBR1^+/CTIP2^+/TBR2^+$ cells at E14.5 and $MEF2C^+/TBR1^+$ cells at E18.5. Cortical regions defined by standardized regions of interest (ROIs) were radially segmented into 10 or 12 equally sized bins of 100 µm width, spanning from the ventricular to the marginal zone. This binning procedure was performed using defined ROI, created by Fiji. The number of marker-positive cells within each bin was quantified, allowing comparison of cellular distribution patterns, in each bin, between genotypes. In addition to cell counting, at E18.5, fluorescence intensity profiles were extracted to evaluate signal distribution across cortical layers. Mean gray-value intensity was measured along the cortical depth to generate representative intensity curves for each condition.

Cell quantification

Quantification of $TRP73^+$, $TBR1^+$, and $RELN^+$ cells at E12.5 was performed across multiple rostro-caudal levels (L1, L2, and L3) to assess distinct subpopulations of CR cells originating from different focal sources and to evaluate their relative contributions. For each coronal section, cell counts were obtained within anatomically matched ROIs placed over the dorso-medial (DM), dorsal (D), dorso-lateral (DL), and lateral (L) pallium in both control and mutant samples. The selection of these specific rostro-caudal levels and the arbitrary subdivision of the pallial regions were adapted from the methodological framework established by (Griveau et al., 2010). The only modification concerns level L3, which we similarly divided into three subregions; however, we labeled them DM, DL, and L, rather than D, DL, and L as in the original study. Positive cells were manually counted within defined ROIs measuring 100 × 100 µm. For each region and for each section, three ROIs were analysed and the mean value was calculated. Counts were carried out separately for $TRP73^+$, $TBR1^+$, and $RELN^+$ cells using Fiji software.

Statistical Analysis

Statistical analyses were performed using GraphPad Prism 9 software, which was also used for data visualization and graphical representation. Data are presented as mean ± standard error of the mean (SEM). Normality of data distribution was assessed using the D'Agostino–Pearson test. Differences between two groups were evaluated using either an unpaired two-tailed Student's *t*-test (for normally distributed data). For analyses involving two independent variables (e.g., genotype and spatial distribution), statistical differences were assessed using a two-way ANOVA. This was followed by Bonferroni post-hoc test to evaluate significance between specific sub-groups. A p-value < 0.05 was considered statistically significant.

Results

-Validation of a novel conditional knockout model for reelin

To achieve conditional deletion of *reelin* expression in the mouse telencephalon across precise spatio-temporal sequence, we combined two different *Cre* driver lines with our *reelin* floxed mouse line (see material and methods). Considering that Cajal-Retzius (CR) *reelin*$^{+}$ cells begin to be produced around E9.5 and are present in the preplate at E10.5, the experimental set up was designed to differentiate between early and late developmental effects, but also to evaluate the distinct contributions of *reelin* expressing cells to the development of the entire telencephalon versus pallial regions. We used *Foxg1-Cre* to ablate the *reelin* expression as E9.5 throughout the telencephalon, and *Emx1-Cre* to delete it starting at E10.5 selectively within the pallium. Using an ubiquitous *Cre* reporter line (*R26R-YFP*) (P. Soriano, 1999; Srinivas et al., 2001), we mapped CRE activity across developmental stages to define the spatial and temporal windows of target deletion. As expected for the *Foxg1*$^{Cre/+}$ line, we detected robust activity throughout the telencephalon (both pallium and subpallium) as early as E9.5 (Fig. S1A-C), sparing only a fraction of YFP-negative cells in the medial pallium—a pattern maintained at E10.5 (Fig. S1D-F, *see asterisk*). In contrast, the *Emx1*$^{Cre/+}$ line showed no detectable CRE activity in the telencephalon (pallium) at E9.5 (Fig. S1A'-C'). The first sparse YFP-positive cells emerged at E10.5, restricted strictly to the medial, dorsal and lateral pallial regions of the pallium in a clear mediolateral gradient (Fig. S1D'-F').

Having verified these *CRE* expression patterns, we next investigated how the resulting conditional knockout (cKO) of exon 3 impacts the *reelin* transcript. First, we excised the *lacZ* cassette, using an ubiquitous *FLP* recombinase mouse line (Farley et al., 2000). To determine the effects of the exon 3 deletion we evaluated *reelin* mRNA and protein expression. Both downstream *in situ* hybridization (exons 37–38) and N-terminal immunostaining (exons 4–5) revealed an absence of reelin in the subpial CR cortical cells of *Reln*$^{fl/fl}$*;Foxg1*$^{Cre/+}$ mice (Fig. 1A-C', D-E'), and a marked reduction in signal and number of reelin^{+} CR cortical cells in *Reln*$^{fl/fl}$*;Emx1*$^{Cre/+}$ mice (Fig. 1F-G', H-I') starting from early stages of development (E12.5).

-Differential reelin mRNA expression across rostro-caudal telencephalic levels at E12.5

To analyse the differential spatio-temporal deletion of *reelin* in our two cKO lines, we selected three rostro-caudal section levels: L1 (through the cortex, striatum and septum), L2 (through the cortex, subpallium and medial pallium) and L3 (through the prethalamic eminence, amygdala and cortex). At E12.5 in *Reln*$^{fl/fl}$*;Foxg1*$^{Cre/+}$ mice, the subpial streams of *reelin*$^{+}$ CR cells were virtually absent across the pallial cortex, as well as within the

septal and striatal domains (Fig. S2A-I'). However, both the mutant and control exhibited a subpial *reelin* signal in a caudal cortical region and in a domain of the amygdalar territory (Fig. S2G-I'). Although this amygdaloid signal lies close to the positive signal from the prethalamic eminence (PThE), cells from the PThE will migrate to that domain only after E12.5 (see discussion). This residual cortical and amygdalar *reelin* positivity can be attributed to cells derived from the cortical hem. Together, these data indicate a dramatic reduction of *reelin* expression from nearly all pallial and subpallial sources.
In contrast, the *Reln*$^{fl/fl}$*;Emx1*$^{Cre/+}$ mice exhibited only a mild reduction of *reelin* positivity in the pallium, with no detectable changes in other regions (Fig. S3). This highlights a significant difference in *reelin* deletion between the two conditional knockout (cKO) lines, demonstrating that the impact of the *Emx1-Cre* line is far less pronounced at this stage than that of the *Foxg1-Cre* line (Figs. S2,S3). Specifically, our data indicates that the *Foxg1-Cre* line eliminates *reelin* starting at E9.5 throughout virtually the entire telencephalon (both pallium and subpallium), including a subset of cells within the cortical hem (Fig. S2). Consequently, all telencephalic sources of CR cells were affected, leaving only the extra-telencephalic PThE intact. Conversely, initiating activity at E10.5, the *Emx1-Cre* line eliminates *reelin* specifically from the cortical hem (Fig. S3).

-reelin loss occurs without impairing CR cell identity at E12.5

Together with *reelin* mRNA analysis, we examined reelin protein expression in both cKO models at E12.5, observing a significant reduction of the RELN signal that strictly correlated with each CRE driver's specific expression domain. To assess the regional distribution of reelin - expressed primarily by Cajal-Retzius (CR) cells at this developmental stage - we analyzed three coronal levels (L1, L2, and L3) along the rostro-caudal axis of the cortex (medial, dorsal and lateral pallium) (Fig. 2). Given that the molecular boundaries of the pallium are poorly defined at E12.5, we systematically partitioned L1/L2 into four sectors (dorso-medial [DM], dorsal [D], dorso-lateral [DL], and lateral [L]), and L3 into three sectors (DM, DL, and L) (Fig. 2). In this framework, DM corresponds to the medial pallium and a portion of the dorsal pallium, D/DL represents the dorsal pallium, and L represents the lateral pallium along with a fraction of the dorsal pallium. This approach enabled the identification of clear spatial Reln expression gradients along the mediolateral axis.
In *Reln*$^{fl/fl}$*;Foxg1*$^{Cre/+}$ mutants, we were unable to detect reelin protein-expressing cells in the cortical regions, precluding formal cell quantification and statistical analysis (Fig. 2A-F'). In contrast, *Reln*$^{fl/fl}$*;Emx1*$^{Cre/+}$ mutants displayed a spatially restricted reelin depletion in regions normally populated by cortical hem-derived CR cells. This reduction was most prominent in the DM, D, and DL sectors—corresponding to the medial and dorsal pallium—across all rostro-caudal levels, whereas the lateral pallium showed minimal reduction confined only to caudal levels (Fig. 2G-O). The pattern of CR reelin depletion

in *Emx1-Cre* mutant is consequence of differing embryonic origins and birth dates: ventral pallium-derived CR cells escape *Emx1-Cre*-mediated recombination, thereby retaining reelin expression to populate mainly the lateral and, occasionally, the dorsal pallium. Furthermore, because *Emx1-Cre* recombination is initiated at E10.5, a fraction of early-born, hem-derived CR cells likely escaped recombination and maintained normal reelin expression.

Together, these findings demonstrate distinct spatio-temporal ablation patterns between the two *reelin* cKO models, explaining the broader phenotype observed in the *Foxg1-Cre* line.

To characterize the CR cells identity in both *reelin* cKO models, we analyzed the spatial distribution of TBR1$^+$ cells (as a pan-CR marker) alongside TRP73$^+$ cells across the four pallial sectors (Fig. 3). TRP73 marks a specific subpopulation of CR cells derived primarily from medial pallium sources—most notably the cortical hem. Previous studies indicate that roughly 75% of reelin expressing CR cells are TRP73$^+$ (Meyer, 2010; Tissir et al., 2009). Although TBR1 is a well-known postmitotic pallial marker, it is also expressed in CR cells (Hevner et al., 2003). In our study, all DM, D, DL and L cortical sectors, pallial septum and some cortical hem TRP73$^+$ cells co-expressed TBR1 (Fig. 3B,D,F). However, some cells from the hem express only TRP73 (Fig. 3F). There were no differences in the total number of TRP73$^+$ and TBR1$^+$ cells between mutants and controls in both cKO models at all cortical sectors, indicating a conserved number of cells in these regions and a similar number of CR cells at least under TRP73$^+$ identity (Fig. S4). This data suggests that CR identity is conserved in mutants even after *reelin* deletion. Next, we analyzed Calretinin (CALB2) expression, a marker of CR cells mainly expressed by most of those cells at E12.5 (Hevner et al., 2003). Our qualitative assessment of the pan-CR marker CALB2 revealed no differences in expression in any pallial subdivision or rostro-caudal level in either *Reln$^{fl/fl}$;Foxg1$^{Cre/+}$* or *Reln$^{fl/fl}$;Emx1$^{Cre/+}$* mutants compared to controls (Fig. S5). Together, these findings indicate that conditional *reelin* deletion causes a regionally patterned loss of reelin protein without compromising CR cell identity or survival at E12.5. Because reelin is essential for guiding migrating neurons during development, this nearly total loss from reelin-positive CR cells is expected to have profound implications for neuronal migration and cortical layer formation in the pallial region.

-Early pan-telencephalic reelin ablation disrupts cortical plate assembly at E14.5

We next assessed the effects of *reelin* deletion on pallium development and validated our *reelin* cKO models, confirming previous data from the *reeler* mouse and other available *reelin* cKO lines (Vilchez-Acosta et al., 2022).

A critical point regarding reelin effects on pallial development is the presence of two primary reelin-expressing neuronal populations: glutamatergic CR cells and GABAergic interneurons. *In situ* hybridization analysis of *reelin* expression between E11.5 and E18.5

revealed these distinct populations within the pallial region (Fig. S6). CR cells localized to the marginal zone across all pallial domains from E11.5 to E18.5 (Fig. S6A-D). Conversely, putative *reelin*$^{+}$ interneurons were initially observed within the mantle zone of the striatal region at E11.5 (Fig. S6A). By E13.5, this signal shifted to the intermediate zone (IZ) of the developing cortex, likely labelling migrating GABAergic interneurons (Fig. S6B). This cortical expression peaked sharply within the IZ at E15.5 before settling into the upper layers by E18.5 (Fig. S6C-D). Collectively, these data suggest that *reelin*$^{+}$ GABAergic interneurons begin populating the cortex between E12.5 and E13.5 (Fig. S6B-C). Moreover, at E14.5 on wild-type brains, we observed sharp *reelin* expression in the marginal zone (denoting resident CR cells) and a secondary signal in the IZ (indicative of migrating interneurons) (Fig. 4A–D).

To evaluate cortical cytoarchitecture at E14.5, we performed Nissl staining on control and mutant neocortices. In *Reln*$^{fl/f}$*;Foxg1*$^{Cre/+}$ mutants, the white matter (WM) boundary separating the cortical plate from the IZ was obliterated, rendering these compartments abnormally continuous compared to heterozygous controls (Fig. 4E–H'). In contrast, *Reln*$^{fl/fl}$*;Emx1*$^{Cre/+}$ embryos appeared largely unaffected (Fig. 4I–L'), consistent with the fact that *Emx1-Cre* spares subcortically derived interneurons and selective pallial cell subsets, leaving these local sources of reelin intact. Collectively, these data show that at E14.5, reelin function is primarily associated with CR cells, with interneuronal contributions expected to become more prominent at early postnatal stages (Vilchez-Acosta et al., 2022).

To further characterize the early *Foxg1-Cre* phenotype in the cortical plate, we analyzed the expression of TBR1, CTIP2, and TBR2 at E14.5 in the dorsal pallium isocortex (Fig. 5). At this transitional stage, TBR1 and CTIP2 are transiently co-expressed in the cortical plate (Fig. 5C). As development proceeds, TBR1 becomes restricted to the earliest-born cortical neurons - including subplate neurons and nascent layer VI - whereas CTIP2 marks subsequently generated layer V projection neurons, and TBR2 identifies intermediate progenitor cells. In control embryos, TBR1 was predominantly localized to the cortical plate, while CTIP2^{+} cells were distributed across both the cortical plate and the IZ, separated by a distinct WM gap. Although the overall distribution of TBR1^{+} neurons was largely preserved in the mutant isocortex, the number of CTIP2^{+} cells was significantly reduced comparing its regional distribution with controls (Fig. 5E,F). This reduction in CTIP2 expression was most pronounced in the IZ, where the migrating stream appeared to abnormally merge with the cortical plate due to the absence of the intervening WM boundary (Fig. 5A,A'). In contrast, TBR2 expression remained comparable between mutants and controls (Fig. 5D,D',G). Collectively, these data indicate that while the earliest-born neuronal populations are maintained with minimal patterning defects, the absence of reelin already impairs the proper migration and lamination of later-born neurons. Moreover, the reduced number of CTIP2^{+} cells in IZ

suggest that the migratory stream has become structurally indistinguishable from the overlying cortical plate.
These findings align with a severe reduction in *reelin* mRNA expression in *Reln$^{fl/fl}$;Foxg1$^{Cre/+}$* mutants compared to controls, although residual signals remained beneath the pial surface of the medial pallium, septum and caudal cortex. We also observed that expression in the PThE—a source of CR *reelin*$^{+}$ cells was maintained in the mutants (Fig.S7).
Collectively, these data demonstrate that early *reelin* expression is essential for proper pallial development.

-Severe disruption of cortical lamination structure at later embryonic stage (E18.5)

In situ hybridization across the rostro-caudal axis of control E18.5 sections confirmed that robust *reelin* expression persists at this late embryonic stage (Fig. S8). Transcripts were particularly prominent in the cortical marginal zone of the dorsal, medial and lateral pallium, providing a spatial reference for the telencephalic territories still subject to *reelin* signaling during late corticogenesis (Fig. S8). Comparing *reelin* mRNA expression between *Reln$^{fl/fl}$;Foxg1$^{Cre/+}$* mutant and controls revealed that at later stages *reelin*-positive CR cells were observed in regions that lacked these cells at E14.5, indicating that CR cells subsequently repopulated these territories, compensating for the initial loss across the subpial dorsal, medial, lateral and ventral cortex, as well as the septal domain (Fig. S9).
To determine the impact of conditional reelin deletion on telencephalic cytoarchitecture during late fetal corticogenesis—a period when *reelin* is still actively expressed—we compared E18.5 coronal sections from control and corresponding cKO mutant (*Reln$^{fl/fl}$;Foxg1$^{Cre/+}$* or *Reln$^{fl/fl}$;Emx1$^{Cre/+}$*) brains using Nissl staining (Fig. S8). In *Reln$^{fl/fl}$;Foxg1$^{Cre/+}$* mutants, Nissl staining revealed a severe and widespread disruption of cortical lamination throughout the rostro-caudal extent of the telencephalon. The CP no longer occupied its normal superficial position; instead, it appeared as an abnormally dense cellular band displaced toward the middle of the cortical wall (Fig. S8D-F'). A similarly prominent defect was observed in the piriform cortex, which exhibited reduced cytoarchitectural differentiation alongside a profound loss of laminar organization (Fig. S8D-E;D'-E''). By contrast, *Reln$^{fl/fl}$;Emx1$^{Cre/+}$* mutants showed no overt cytoarchitectural alterations in either the dorsal pallium or the piriform cortex at this stage, with laminar architecture remaining largely preserved across all rostro-caudal levels examined (Fig. S8G-I').

To further study cortical lamination at E18.5 following conditional *reelin* deletion, we examined the distribution of selected layer-specific markers, using MEF2C as an indicator of superficial layers and TBR1 as a marker of layer I and deep-layer neurons. In

Reln$^{fl/fl}$*;Foxg1*$^{Cre/+}$ cKO brains, we observed a profound alteration of cortical stratification (Fig. 6A-C'). Quantitative analyses confirmed a severe loss of normal laminar organization, with both MEF2C and TBR1 signals aberrantly redistributed throughout the entire radial dimension but preferentially concentrated toward superficial cortical regions (Fig. 6A',B'). Notably, TBR1 expression exhibited an inverted pattern relative to its normal deep-layer localization, indicating a severe mispositioning of early-born neurons (Fig. 6B,B',E,G). While MEF2C was heavily concentrated near the surface, it was also broadly scattered throughout the cortex in these mutants (Fig. 6A,A',D,F). Furthermore, whereas control brains exhibited a population of layer VI cells co-expressing MEF2C and TBR1, this dual-positive population was localized close to the surface in the mutant (Fig. 6C,C'). Consistent with previous reports in the *reeler* mouse, cortical lamination defects in *Reln*$^{fl/fl}$*;Foxg1*$^{Cre/+}$ cKO followed a rostro-caudal gradient, with caudal sections displaying a more prominently inverted pattern (*data not shown*; Boyle et al., 2011; Mingo-Moreno et al., 2024).
In contrast, *Reln*$^{fl/fl}$*;Emx1*$^{Cre/+}$ cKO brains showed no overt lamination defects, though a subtle alteration - characterized by a decreased number of TBR1^{+} cells - was detected around layers I/II and IV/V (Fig. S10).

-Severe disruption of cortical lamination structure at postnatal stage P30

To determine if the defects resulting from early *reelin* ablation in the telencephalon persist or resolve at later stages - after the majority of the CR cells disappeared (Chowdhury et al., 2010; Derer & Derer, 1990) - we examined the cytoarchitecture of postnatal day 30 (P30) *Reln*$^{fl/fl}$*;Foxg1*$^{Cre/+}$ cKO mice. Nissl staining revealed profound and permanent disruptions across mature cortical and limbic structures. In the isocortex - a dorsal pallial derivative - laminar organization was disrupted, marked by a total loss of layer I and an absence of distinct layers (Fig. 7A,A'). Similarly, lamination was altered in the piriform cortex (derived from the ventral pallium), which displayed only sparse differentiated neurons, reflecting impaired cellular migration (Fig. 7B,B').
Next, we focus on allocortical territories characterized by a three-layered cytoarchitecture: the taenia tecta and the indusium griseum. Anatomically, the TT is positioned rostral to the corpus callosum (cc), while the IG extends caudally from the TT, running dorsal to the cc until it transitions into the hippocampal formation at its caudal boundary. These medial pallium-derived telencephalic structures were severely compromised in *Reln*$^{fl/fl}$*;Foxg1*$^{Cre/+}$ mutants. The TT was absent, resulting in a complete loss of their characteristic neuronal populations and layered organization (Fig. 7E,E'). Moreover, the normally compact bilateral cell clusters of the IG were cytoarchitectonically indiscernible (Fig. 7D,D'). This apparent absence reflects a profound failure of neuronal condensation; instead of forming a cohesive structure dorsal to the enlarged cc, the cellular elements remain loosely scattered.

The hippocampal formation, another medial pallial derivative, exhibited severe dysgenesis. Compared with the well-organized cytoarchitecture of control animals, *Reln*$^{fl/fl}$*;Foxg1*$^{Cre/+}$ mutants displayed profound disruption of hippocampal morphology. The dentate gyrus (DG), Cornu Ammonis 1 and 3 (CA1, CA3) regions lacked their characteristic layered organization and exhibited severely disorganized cellular architecture, consistent with a failure in normal hippocampal development (Fig. 7C,C'). Nevertheless, this structural disruption was less severe than that observed in the TT and IG, allowing the broad identification of the CA subfields.

In contrast, cytoarchitectural analysis of *Reln*$^{fl/fl}$*;Emx1*$^{Cre/+}$ mice at P30, showed that, unlike the severe, canonical *reeler*-like disruptions observed in *Foxg1*-Cre mutants, Nissl staining of mature *Emx1*-Cre brains revealed no detectable qualitative structural alterations across the telencephalon (Fig. S11). Specifically, coronal sections showed a fully preserved, six-layered isocortical stratification, indicating that any subtle architectural differences, if present, fell below the resolution of this analysis (Fig. S11A,A'). The piriform cortex also maintained its characteristic three-layered organization, with no signs of ectopic cellular displacement or lamination defects (Fig. S11B,B'). Further examination of medial pallial derivatives confirmed the absence of structural defects. The hippocampal formation displayed normal morphogenesis, with the CA1, CA2 and CA3 subfields and the DG forming tightly packed, correctly positioned neuronal layers (Fig. S11C,C'). Along the midline, the cc properly crossed the interhemispheric fissure without any evidence of dysgenesis. Consistently, the IG and TT successfully condensed into characteristic, compact structures dorsal to the cc and along the medial wall, respectively (Fig. S11D-E'), lacking the severe cellular scattering and structural collapse that characterize broad, *Foxg1*-Cre-mediated *reelin* deletion. Collectively, these adult findings confirm that restricting *reelin* ablation to the dorsal pallium via *Emx1*-Cre is insufficient to trigger gross lamination or midline condensation defects, at mature postnatal stages.

-Molecular phenotyping reveals severe iso- and allocortical impairment

To characterize the molecular basis of the anatomical defects observed at P30, we focussed our analysis on *Reln*$^{fl/fl}$*;Foxg1*$^{Cre/+}$ mice, which exhibited the more severe phenotype. To this end, we examined the expression of specific regional markers - *Lpl*, *Lmo3, Slit2*, and *Zbtb20* - at E18.5 to identify the early developmental events driving these alterations. In the isocortex of control brains, both *Lpl* and *Lmo3* prominently labeled the expected superficial layers (Fig. 8D,G; Fig. S12). Conversely, in *Reln*$^{fl/fl}$*;Foxg1*$^{Cre/+}$ mutants, the expression domains of these markers were ectopically shifted toward the central portion of the cortical wall, consistent with the abnormal redistribution of neurons observed via Nissl staining (Fig. 8A',D',G'; Fig. S12). Furthermore, the *Lmo3* expression

domain in mutants displayed a striking regional shift along the medio-lateral axis: its signal was noticeably downregulated in areas adjacent to the medial pallium, while appearing laterally displaced and more prominent within the lateral pallium (Fig. 8B,B'; Fig. S12). This structural disorganization in *Reln*$^{fl/fl}$*;Foxg1*$^{Cre/+}$ mutants extended ventrally into the piriform cortex, a ventral pallial derivative, which exhibited profound differentiation defects. In this region, the typically widespread *Lpl* labeling was severely reduced and confined to a discrete, compact cluster in mutant brains (Fig. 8E,E'; Fig. S12F,F'). The well-defined, stratified expression profile of *Lmo3* observed in controls was entirely replaced by a single broad, diffuse band (Fig. 8H,H'; Fig. S12B-D'). Importantly, these molecular markers uncovered striking abnormalities within the medial pallium-derived hippocampal formation that were not readily discernible by Nissl staining alone (Fig. 8C,C'). While controls displayed highly organized and coherent expression bands across all hippocampal subfields, mutants exhibited widespread neuronal dispersion. Specifically, while *Lpl* (delineating the CA2 and CA3 fields) and *Lmo3* (defining the CA1 region) remained localized to their general expected layers, their signals were broadly diffused into neighboring strata - such as the *strata pyramidale* and *oriens* - rather than being tightly clustered (Fig. 8F,F',I,I';Fig. S12D,D',H,H'). In addition, *Slit2* expression was markedly altered in *Reln*$^{fl/fl}$*;Foxg1*$^{Cre/+}$ mutants. In control embryos, *Slit2* outlined the characteristic morphology of the dentate gyrus (DG) and defined a distinct, curved CA1-associated stripe continuous with the subicular and entorhinal cortices. In mutants, however, *Slit2* signal was highly diffuse throughout the area and failed to resolve the typical structural configuration of the DG; furthermore, the CA1 region and the subicular/entorhinal cortex completely lacked the distinct, *Slit2*-positive line observed in controls (Fig. 8J-J'). This defective hippocampal lamination was further corroborated by *Zbtb20*—a robust marker for the developing DG and the CA sectors—which similarly displayed an altered pattern that was particularly severe in the DG (Fig. 8K,K'). Together, these molecular readouts underscore profound, widespread defects in neuronal migration and cellular positioning across the developing pallium and the hippocampal formation.

-Altered Morphogenesis of rostral medial pallial derivatives in Foxg1-Cre mutants at E18.5

We then focused on the most rostral medial pallial derivatives—the TT and IG)—as the reelin deletion phenotype in these regions was not described before. At E18.5, the molecular identity of these medial pallial derivatives is clearly defined in controls by *Zbtb20* expression (Fig. S13D-F,E',F'). Furthermore, *Peg10* is expressed in subsets of cells within both the TT/IG and the hippocampal CA3 region, suggesting a shared molecular profile between these territories (Fig. S13A-C,B',C').

To investigate the structural organization of the TT and IG at E18.5, we combined immunohistochemistry for TBR1 and CTIP2 but also analyzed the *ISH* pattern for the specific transcripts *Zbtb20*, *Lmo3*, *Peg10*, *Lpl* and *Slit2*. Overall, our data indicate that while mutant medial pallial neurons maintain their pallial molecular identity, their radial organization is severely disrupted. In control animals, TBR1$^+$ cells span the entire radial dimension of both the TT and IG, with the majority of these neurons concentrated in the intermediate layer, adjacent to the stratum moleculare near the pial surface (Fig. 9C,F,I). A small cell population of CTIP2$^+$ cells is also observed within the TT (Fig. 9B,E). In contrast, the TT of *Reln$^{fl/fl}$;Foxg1$^{Cre/+}$* mutants exhibit a complete alteration of lamination, with TBR1$^+$ and CTIP2$^+$ cells broadly distributed across the entire radial dimension (Fig. 9B',C',E',F'). The well-ordered cellular ribbon of the intermediate layer seen in controls is replaced by a large disturbed postmitotic mantle layer of TBR1$^+$ and CTIP2$^+$ neurons. Due to this severe failure of condensation, these scattered cells remain distributed without any preferential position (Fig. 9B',C',E',F'). In mid-caudal coronal planes - at the level of the corpus callosum crossing - control TBR1$^+$ neurons aggregate compactly to form the IG, appearing as dense bilateral bands resting directly in a supracallosal or dorsal position. Conversely, the loss of reelin in mutant embryos prevents TBR1$^+$ neurons from assembling into these tight superficial laminae, resulting instead in a dispersed, disorganized lamination distributing throughout the mantle layer (Fig. 9G-I').
This dramatic scattering phenotype within the IG and TT in the *Reln$^{fl/fl}$;Foxg1$^{Cre/+}$* mutants was further corroborated by *ISH* analysis. In control embryos, *Lmo3* expression strongly labeled the TT and was readily detectable in the IG (Fig. 10A-D). In mutants, however, this signal was drastically reduced, becoming nearly undetectable in the TT and visibly diminished in the intermediate layer of the IG (Fig. 10A'-D'). Similarly, *Zbtb20* mRNA expression in controls was predominantly concentrated in the intermediate layer of both the TT and IG (Fig. 10 E-H). Furthermore, rather than forming the compact domain observed in controls, the mutant TT and IG exhibited an elongated, dispersed configuration spanning the entire radial dimension (Fig. 10E'-H'). In contrast to the compact *Peg10* signal that distinctively demarcates the TT and IG in controls, mutant expression was diffuse and disorganized (Fig. 11A-C'). Likewise, *Lpl* transcript analysis confirmed a broadened radial distribution and a failure of IG compaction (Fig. 11D-F'). Together, these rostro-caudal observations demonstrate that reelin is essential for the spatial compaction and laminar assembly of the TT and IG, without apparently altering the biochemical specification of their constituent neuronal populations.

-Severe disorganization of Nr4a2 expression in the claustrum, dorsal pallial cortex, subplate and subiculum, of Foxg1-Cre mutants at E18.5

To further characterize the effects of widespread reelin ablation across pallial regions, we analyzed the expression of *Nr4a2* (*Nurr1*), focusing on structures whose development

relies heavily on precisely regulated neuronal migration: the claustrum, the subplate and the subiculum (Sub). At E18.5, *Nr4a2* robustly labels the claustrum proper (Clp) in the lateral pallium and the underlying endopiriform dorsal nucleus (EpD) in the ventral pallium, reflecting their shared origin from lateral pallial progenitors (Fig. 12A-C). Additionally, *Nr4a2* transcripts demarcate subplate cells throughout the dorsal and lateral pallium, neurons within the CP (predominantly clustered in the parietal cortex), and cells flanking the subicular region (Fig. 12A-C and Fig. S14A-J). In *Reln*$^{fl/fl}$*;Foxg1*$^{Cre/+}$ mutants, however, the *Nr4a2* signal within the Clp was markedly weaker and more diffuse, occupying a broader radial dimension than in controls (Fig. 12A'-C'; Fig. S14A'-J'). This altered distribution suggests that the claustrum fails to condense properly within its deep position beneath the insular cortex. Notably, a distinct population of *Nr4a2*$^{+}$ cells appeared ectopically intermixed within the insular cortex itself (Fig. 12A'). Furthermore, *Nr4a2* expression in the mutant EpD was severely attenuated and sparse (Fig. 12A'-C'; Fig. S14A'-H').

Beyond the claustrum, the distinct, thin band of subplate-associated *Nr4a2* expression was entirely lost in *Reln*$^{fl/fl}$*;Foxg1*$^{Cre/+}$ mutants. Similarly, the compact *Nr4a2* signal characteristic of the control outer CP (primarily within the parietal cortex) was disorganized in the mutant cortex (Fig. 12A-B,A'-B'; Fig. S14A-F,A'-F'). Instead of forming a restricted layer, *Nr4a2*$^{+}$ cells were broadly scattered across the radial axis, with many remaining trapped in deep layers and failing to reach their superficial destinations. This distribution highlights a profound radial positioning defect among *Nr4a2*$^{+}$ neocortical neurons.

Comparable alterations were evident within the hippocampal formation, specifically in the region corresponding to the subiculum. In control embryos, *Nr4a2* expression was sharply concentrated within the subiculum (Fig. 12B). In *Reln*$^{fl/fl}$*;Foxg1*$^{Cre/+}$ cKO embryos, however, this domain appeared visibly diminished and dispersed, characterized by a lower density of *Nr4a2*$^{+}$ neurons and a loss of normal compact stratification (Fig. 12B'). Together, these observations indicate that widespread reelin ablation disrupts the structural organization and spatial positioning of multiple *Nr4a2*$^{+}$ telencephalic domains, demonstrating that reelin function extends beyond neocortical lamination to play an essential role in the spatial organization and structural compaction of both the claustrum and the subiculum during late embryogenesis.

Discussion

The process of mammalian corticogenesis requires precise spatio-temporal control of signaling molecules that regulate the formation of the structural architecture of the adult cortex. Among these signals reelin serves as an indispensable key regulator. By leveraging conditional loss-of-function genetic strategies this study provides a high-

resolution dissection of the spatial and temporal effects of reelin signaling across the developing telencephalon. Our findings not only validate a novel conditional knockout line but mainly shed new light on the early role of reelin in shaping diverse pallial derivatives.

-Characterization of the reelin cKO model

Initial studies on the role of reelin during brain development were conducted using a constitutive *reeler* knockout model (Arcangelo & Curran, 1998). Starting from ES cells carrying a conditional allele a *Reln*^{fl} allele as in (Cionni et al., 2016), we generated a novel conditional *Reln* mouse line that we used to generate a high-resolution dissection of the spatial and temporal roles of reelin across the developing telencephalon. To specifically eliminate major telencephalic sources of reelin^{+} cells, we crossed *Reln*^{fl} mice with the *Foxg1-Cre* line - for the first time - alongside the *Emx1-Cre* line as was performed by others (Cionni et al., 2016). Other studies were performed using a floxed *Reln* exon 1 variant and have investigated reelin ablation in CALB^{+} cells (*Calb2-Cre*), or the ubiquitously in the brain (*CAG-CreERT2*) and from GABAergic interneurons (*Gad2-Cre*; *Dlx5/6-Cre*) (Lane-Donovan et al., 2015; Pahle et al., 2019; Schneider-lódi et al., 2025; Vilchez-Acosta et al., 2022). Our approach contrasts broad forebrain-wide deletion with dorsal pallium-restricted ablation to systematically evaluate regional requirements.
reelin ablation is expected to be equivalent in both exon 1 and exon 3 floxed lines, as neither line exhibits detectable *reelin* mRNA or protein expression (Vilchez-Acosta et al., 2022; present study). In our exon 3 line, complete loss was confirmed by *ISH* (exon 37–38 riboprobe) and immunodetection (exon 4–5 epitope antibody), which is consistent with the lack of functional start codons downstream of exon 3. In this study, we took advantage of two different CRE driver lines, to dissect the spatial- and temporal-specific role of reelin during pallial development.
reelin is a protein secreted by CR cells, the first neurons to differentiate in the pallium. Quantitative co-expression data in the mouse telencephalon indicate that 70–75% of reelin^{+} CR cells co-express TRP73, primarily as the DeltaNp73 isoform (Tissir et al., 2009). As reviewed by (Meyer, 2010), ~98% of TRP73^{+} CR cells co-express reelin. Also, TBR1 is robustly expressed in CR reelin^{+} cells (Hevner et al., 2001). At E12.5, our quantitative expression analysis of CALB2, TRP73, and TBR1 confirmed that loss of reelin in conditional knockouts (using *Foxg1-Cre* or *Emx1-Cre* drivers) does not alter CR cell specification, survival, or early spatial distribution. These findings align with previous CALB2-based studies in classic *reeler* mice (Ogawa et al., 1995) and match the preserved TBR1 expression observed in the *reeler* (*Reln*$^{-/-}$) cortex during cortical development (Hevner et al., 2001). Collectively, these data highlight that the observed phenotypes stem directly from absent reelin signaling rather than secondary CR cell death or misspecification. Conversely, it was demonstrated that loss of TRP73 selectively reduces the number of reelin-positive CR cells in the caudal telencephalon,

demonstrating that TRP73 is required to specify hem-derived CR reelin$^+$ cell fate (Meyer et al., 2004).

-Differential effects in cKO models using Foxg1-Cre and Emx1-Cre lines

CR cells are glutamatergic, *reelin*$^+$ neurons located subpially across all pallial regions, and generated primarily between E10.5 (80%) and E12.5 (20%) (Alcántara et al., 1998; Bielle et al., 2005; Hevner et al., 2003). Additionally, reelin in cortical pallial domains is produced by GABAergic interneurons that begin migrating from the subpallial ganglionic eminences at E12.5 (Fig. S6);(Kelsom & Lu, 2013; Parnavelas, 2000). The robust telencephalic reelin ablation achieved via *Foxg1-Cre* by E12.5 - encompassing the loss of both reelin$^+$ CR cells and interneurons - reflects early *Foxg1* expression across pallial and subpallial domains starting at E9.5 (Hébert & McConnell, 2000). However, starting at E14.5, we observed a minimal repopulation of CR *reelin*$^+$ cells in the caudal cortex, septum and medial pallium. This compensation likely stems from incomplete *Foxg1-Cre* recombination in the cortical hem, as well as the preservation of *reelin*$^+$ CR cells originating from the PThE. Indeed, the PThE has been identified as the key source of *reelin*$^+$ CR cells that migrate into the telencephalon, populating the piriform, entorhinal, and somatosensory cortices, as well as the ventral forebrain, between E14.5 and E15.5 (de Frutos et al., 2016; Ruiz-Reig et al., 2016; Ruiz-Reig & Studer, 2017; Tissir et al., 2009).

Whether the transcription factor Foxg1 acts as a potent repressor of *reelin*$^+$ CR cells lineage was initially controversial (Hanashima et al., 2004; Muzio & Mallamaci, 2005). However, subsequent studies demonstrate that conditional deletion of *Foxg1* at E13.5 redirects progenitors towards a CR fate rather than pyramidal neuron fate (Hanashima et al., 2007; Kumamoto et al., 2013). Furthermore, Foxg1 represses key downstream genes required for CR development - including *Ebf2/3* and *Dmrta1/Dmrt3* - whereas forced *Foxg1* expression in the cortical hem shifts cell fate from CR neurons to dentate granule neurons (Kikkawa et al., 2020; Liu et al., 2018). Given that Foxg1 dosage directly influences CR lineage specification, we exclusively utilized a *Foxg1-Cre* knock-in allele and rigorously compared $Reln^{fl/fl};Foxg1^{Cre/+}$ conditional mutants against heterozygous controls harboring the same single *Foxg1* functional allele.

To evaluate regional *reelin* requirements, $Reln^{fl}$ mice were also crossed with the *Emx1-Cre* line, which drives CRE expression specifically within medial, dorsal and lateral pallial lineages. In contrast to the severe phenotype observed in $Reln^{fl/fl};Foxg1^{Cre/+}$ mouse, $Reln^{fl/fl};Emx1^{Cre/+}$ mutants exhibited a significantly milder phenotype. This difference is explained by the later onset of *Emx1-Cre* activation (from E10.5 onwards; (Briata et al., 1996)) and its restricted expression domain which spares key sources of reelin$^+$ CR

cells—such as the septal pallial, ventral pallium and prethalamic eminence territories—as well as migrating inhibitory interneurons.

-Effect of this mutant vs reeler and other mutants in the lamination of the cortical pallial derivatives

At E14.5, the isocortex of *Reln$^{fl/fl}$;Foxg1$^{Cre/+}$* mutants exhibit a complete loss of the CP–IZ boundary. This architectural collapse uncovers a lineage-specific phenotype: early-born TBR1^{+} subplate and layer VI neurons show normal spatial organization, whereas migrating CTIP2^{+} layer V projection neurons are severely depleted and disorganized. Because TBR1^{+} cells transiently co-express CTIP2 at this stage, the selective loss of CTIP2^{+} neurons and IZ demonstrates that later-born lineages uniquely depend on reelin to navigate past earlier-born layers. Consequently, *inside-out* migration fails, trapping later-born neurons within the subplate and obscuring the WM boundary. These phenotypes are mostly plausibly driven by the absence of reelin from CR neurons.
Usually, *reelin* expression in cortical layer I is restricted to CR cells between E11.5 and E18, with expression in GABAergic interneurons emerging around E18.5 (Alcántara et al., 1998; Supèr et al., 1998). However, while interneuronal *reelin* mRNA was previously reported to emerge in the CP only at E17–E18 (Alcántara et al., 1998), our data show that CP *reelin* expression starts as early as E13.5, resolving into distinct superficial and deep layer profiles by E15.5–E18.5.
Indeed, CR cell-derived reelin orchestrates early *inside-out* cortical lamination, whereas interneuron-derived reelin is largely dispensable during initial migration and functions later to restrict layer I invasion (Vilchez-Acosta et al., 2022). This central role is reinforced by ectopic expression studies, which demonstrate that reelin alone can induce a cell-body-sparse zone and birthdate-dependent *inside-out* alignment of neuronal organization in the developing isocortex (Kubo et al., 2010). Additionally, global reelin loss in *reeler* mutants disrupts neocortical development, leading to failed preplate splitting, subplate displacement, and cortical migration defects; at early stages, these impairments are primarily attributable to the loss of CR-derived reelin (Mingo-moreno et al., 2024).
Pan-telencephalic deletion of *reelin* (*Reln$^{fl/fl}$;Foxg1$^{Cre/+}$*) causes severe, *reeler*-like laminar disruption from E18.5 (*Mef2c, Lpl, Lmo3*, *Tbr1, and Nissl staining*) through P30 (Nissl staining), without altering overall cortical thickness (data not shown). This confirms that reelin primarily regulates spatial positioning rather than neurogenesis or cell survival. Conversely, although *Reln$^{fl/fl}$;Emx1$^{Cre/+}$* mutants exhibit minimal disorganization at E18.5, their P30 brains display wild-type isocortical lamination and hippocampal architecture, suggesting compensation for the early *reelin* deletion *Reln$^{fl/fl}$;Emx1$^{Cre/+}$* phenotype at later stages. This is in line with the current literature, in which is described that hem ablation does not compromise lamination in the neocortex (Yoshida et al., 2006), as also

demonstrated in *Gmnc*$^{-/-}$ (Elorriaga et al., 2025) and *Trp73*$^{-/-}$ mutants (Meyer et al., 2004). Spared reelin production from subpallial interneurons, together with residual hem-derived and ventral pallial CR cells is thus sufficient to rescue fine-scale neuronal placement postnatally. These findings align with previous work showing that the selective loss of reelin in CR cells - with minimal contribution from interneurons - alters *inside-out* lamination (Vilchez-Acosta et al., 2022).

A similar phenotype is observed in mutants affecting the reelin signaling pathway. The reelin intracellular effector DAB1 is strictly required for the radial translocation of neurons past early-born layers into the outer CP (Cooper, 2008; Sekine et al., 2011). Without functional reelin or DAB1 signaling, preplate splitting fails; the subplate is misplaced, and migrating neurons crowd below it, eliminating the distinct boundary zone between the CP and IZ across multiple regions of the *reeler* and *Dab1*-deficient brain (Mingo-moreno et al., 2024; Yoshinaga et al., 2022). Consistently, loss of the reelin receptor ApoER2 similarly impairs the migration of late-generated neurons (Hack et al., 2007), demonstrating a role for the reelin signaling pathway in regulating cortical assembly.

Beside the well-known defects in the isocortex, reelin deficiency severely impairs development of the medial pallial allocortex. In *Reln*$^{fl/fl}$*;Foxg1*$^{Cre/+}$ mutants, TBR1^{+} and CTIP2^{+} neurons in the TT and IG fail to undergo radial compaction, displaying disorganized expression of *Zbtb20, Lmo3, Peg10* and *Lpl*. Similar, albeit milder, condensation defects across CA1 (*Lmo3*$^{+}$*, Lpl*$^{+}$*, Slit2*$^{+}$), CA2/CA3 (*Lpl*$^{+}$), and the DG (*Zbtb20*$^{+}$*, Slit2*$^{+}$) demonstrate that reelin is broadly required for allocortical lamination. The relatively milder phenotype in the DG aligns with the known loss of reelin in CR cells, which compromises the radial glial scaffold and layer integrity in *reeler* mice (Frotscher et al., 2003; Sibbe et al., 2009; Zhao et al., 2004). Furthermore, reelin-DAB1 signaling is critical for lamination of the hippocampal proper, as DAB1-deficient mice exhibit differential laminar disruptions in CA1/CA3 compared to the DG (Blume et al., 2017). Collectively, these data indicate that reelin regulates allocortical lamination and neuronal compaction across medial pallial derivatives. However, severe defects in the TT and IG, allocortical derivatives part of the limbic system located rostral to the hippocampus proper, have not been previously described. Further studies are needed to determine the molecular mechanisms underlying this phenotype in the *Reln*$^{fl/fl}$*;Foxg1*$^{Cre/+}$ mutants and to compare these anterior medial pallial defects with those observed in the DG, a caudal medial pallium derivative. The heightened vulnerability of the TT and IG relative to the hippocampus proper (CA fields and DG) observed in *Reln*$^{fl/fl}$*;Foxg1*$^{Cre/+}$ mutants may stem from spatial and temporal gradients in reelin delivery: an early, complete absence of reelin in the topologically most rostral domains (TT and IG), contrasted with potential late repopulation by reelin^{+} CR cells in the more caudally situated hippocampus proper.

Finally, reelin deficiency impairs both nuclear compaction and lamination within lateral and ventral pallial derivatives at E18.5. In control brains, *Nr4a2* (*Nurr1*) demarcates the compact Clp and EpD claustral components, which are derived from the lateral pallium,

but located in the lateral and ventral pallium, respectively (Puelles et al., 2016). In contrast, *Reln*$^{fl/fl}$*;Foxg1*$^{Cre/+}$ mutants exhibit a weakened, diffused *Nr4a2* expression profile, with ectopic cells scattered into the insular cortex and a disrupted pattern throughout the EpD. Additionally, *Nr4a2* expression—normally present in the subplate and specific layers of the somatosensory cortex in controls (Bruguier et al., 2020; Puelles, 2014; Puelles et al., 2016)—is absent from the subplate and severely malpositioned within the isocortex of mutants suggesting an impaired tangential migration from the lateral pallium. The structural disruption of the Clp and EpD in *Reln*$^{fl/fl}$*;Foxg1*$^{Cre/+}$ mutants is noticeably milder than that observed in global *reeler* mice, a divergence most likely attributable to the repopulation or compensation by reelin-expressing CR neurons (Oshima et al., 2023). Therefore, the present results suggest that the *Nr4a2* positive cells fail to migrate properly to the subplate and maintain malpositioned close to the dorsal Clp. Coupled with disorganized *Lpl* and *Lmo3* expression in the three-layered piriform cortex, these results demonstrate a universal requirement for reelin in driving nuclear condensation and laminar segregation throughout the telencephalon. Together, these data establish that reelin signaling is fundamentally required not only for neocortical inside-out lamination, but also for nuclear assembly and structuring of diverse pallial domains.

Summary

Together, these findings establish that reelin functions as a general regulator of the neuronal architecture within distinct pallial domains, extending far beyond its classical role in inside-out neocortical lamination (Boyle et al., 2011; D'Arcangelo et al., 1995). By orchestrating both radial lamination in the limbic medial pallial allocortex (hippocampus, taenia tecta, and indusium griseum) and nuclear condensation within early-born lateral and ventral pallial derivatives, reelin governs fundamental, multi-regional principles of forebrain assembly (Mingo-moreno et al., 2024). Ultimately, the disruption of mesocortical and allocortical as well as isocortical disorganization underscores that reelin signaling is required for both laminar segregation and non-laminar nuclear positioning throughout the entire telencephalon and therefore has a more general role on the establishment of neuronal organization in the telencephalon.

Acknowledgments

We thank Prof. John Parnavelas for starting the project with the generation of the Reln^{flx} line. We also thank Andrea Marini for help in data generation and Cinzia Valente for animal care.

Author contributions

E.L. Crapanzano and U. Borello designed the study; E.L. Crapanzano performed the experiments; E.S. Bacci assisted in performing the experiments; M. Barber generated the Reln floxed line; C. Gabellini, E.L. Crapanzano, J.L. Ferran, U. Borello data analysis and paper writing. All the authors revised the manuscript.

Funding

This work was supported by the PNRR ECS00000017—'THE – Tuscany Health Ecosystem'—Spoke 6 'Precision medicine & personalized healthcare', CUP I53C22000780001, funded by the European Commission under the NextGeneration EU program.

Figure legends

Fig.1. Differential effects of *Reln* deletion in two conditional knockout models (cKO). (A) Schematic representation of the *Reln* genomic locus showing the relative position of the *ISH* probe (spanning exons 37 and 38), the loxP sites flanking the targeted region (black triangles), RELN antibody epitope between exon 4 and 5 (black line) along with the exon/intron *Reln* gene model. (B–B') Representative section of *In situ* hybridization for *Reln* mRNA in control brain $Reln^{fl/+};Foxg1^{Cre/+}$ and mutant brain $Reln^{fl/fl};Foxg1^{Cre/+}$;(C-C') higher-magnification view of the dorsal pallium shown in B-B'. (D–D') Representative section of *in situ* hybridization for *Reln* mRNA in control brain $Reln^{fl/+};Emx1^{Cre/+}$ and mutant brain $Reln^{fl/fl};Emx1^{Cre/+}$;(E-E') higher-magnification view of the dorsal pallium shown in D-D'. (F–F') Representative section of immunofluorescence for RELN protein in control brain $Reln^{fl/+};Foxg1^{Cre/+}$ and mutant brain $Reln^{fl/fl};Foxg1^{Cre/+}$;(G-G') higher-magnification view of the dorsal pallium shown in F-F'. (H–H') Representative section of immunofluorescence for RELN protein in control brain $Reln^{fl/+};Emx1^{Cre/+}$ and mutant brain $Reln^{fl/fl};Emx1^{Cre/+}$;(I-I') higher-magnification view of the dorsal pallium shown in H-H'. Cx, Cortex; Se, Septum; St, Striatum. Scale bars: 100 µm for the overview panels and 50 µm for the higher-magnification immunofluorescence panels.

Fig. 2. Immunofluorescence for TBR1 and RELN in the dorsal pallium across the rostro-caudal axis at E12.5. (A-F) Representative coronal sections from control $Reln^{fl/+};Foxg1^{Cre/+}$ and (A'-F') mutant $Reln^{fl/fl};Foxg1^{Cre/+}$ embryos at three rostro-caudal levels (L1, L2, and L3). (G-L) Representative coronal sections from control $Reln^{fl/+};Emx1^{Cre/+}$ and (G'-L') mutant $Reln^{fl/fl};Emx1^{Cre/+}$ embryos at the same levels. Boxed areas are shown at higher magnification. At L1 and L2, the dorsal pallium was subdivided into four selected bins: dorso-medial (DM), dorsal (D), dorso-lateral (DL), and lateral (L). At L3, three zones were analyzed (DM, DL, L). Scale bars: 100 µm. (M-O) Quantification of the number of $RELN^+$ cells per selected bins at each rostro-caudal level in *Emx1-Cre* experimental groups. Data are presented as mean ± SEM. Statistical comparisons were performed using two-tailed unpaired Student's t-test; ****$p < 0.0001$; ***$p < 0.001$; **$p < 0.01$; *$p < 0.05$. n = 3 embryos/genotype.

Fig. 3. Immunofluorescence analysis of TBR1 and TRP73 in the dorsal pallium across the rostro-caudal axis at E12.5. (A-L') Representative coronal sections at three rostro-caudal levels (L1, L2, and L3) from control $Reln^{fl/+};Foxg1^{Cre/+}$ (A-F) and mutant $Reln^{fl/fl};Foxg1^{Cre/+}$ (A'-F') as well as control $Reln^{fl/+};Emx1^{Cre/+}$ (G-L) and mutant $Reln^{fl/fl};Emx1^{Cre\ /+}$ (G'-L') embryos. Boxed areas indicate regions shown at higher magnification. At L1 and L2, the dorsal pallium is subdivided into four selected bins: dorso-medial (DM), dorsal (D), dorso-lateral (DL), and lateral (L). At L3, three levels were

analyzed (DM, D, DL). High-magnification panels detail the dorsal cortex (in B), pallial septum (in D), and cortical hem (in F). White arrows indicate TBR1/TRP73 double-positive cells, whereas blue and orange arrows point to cells expressing only TBR1 or TRP73, respectively (highlighted in F). PalSe, pallial septum. n = 3 embryos per genotype. Scale bars: 100 µm.

Fig. 4. *reelin* expression and cytoarchitectural organization of the two cKO developing forebrain at E14.5. (A–D) *In situ* hybridization showing *Reln* mRNA expression in representative sections of the wild-type (WT) forebrain. (E–L') Cytoarchitectural organization of the developing dorsal pallium revealed by Nissl staining. Representative coronal sections at distinct rostro-caudal levels are shown for control *Reln*$^{fl/+}$;*Foxg1*$^{Cre/+}$ (E-H) and mutant *Reln*$^{fl/fl}$;*Foxg1*$^{Cre/+}$ (E'-H') embryos, as well as for control *Reln*$^{fl/+}$;*Emx1*$^{Cre/+}$ (I-L) and mutant *Reln*$^{fl/fl}$;*Emx1*$^{Cre/+}$ (I'-L') embryos. High-magnification views of the dorso-lateral pallium (F, F', H, H', J, J', L, L') highlight the structural organization of the cortical plate (CP). VZ, ventricular zone; IZ, intermediate zone; CP, cortical plate; WM, white matter. *n* = 3 embryos per genotype. Scale bars: 500 µm.

Fig. 5. Cortical distribution of CTIP2$^+$, TBR1$^+$ and TBR2$^+$ cells at E14.5 in control and mutant mice. (A–D') Cortical distribution of CTIP2$^+$, TBR1$^+$, and TBR2$^+$ cells at E14.5 in *Reln*$^{fl/+}$;*Foxg1*$^{Cre/+}$ and *Reln*$^{fl/fl}$;*Foxg1*$^{Cre/+}$ mice. (A-A') Representative images show CTIP2 single channel, (B-B') TBR1 single channel, CTIP2/TBR1 merge, and TBR2 single channel. (C-C') In the CTIP2/TBR1 merge, TBR1-only-positive cells are marked by asterisks. SVZ, subventricular zone; VZ, ventricular zone; IZ, intermediate zone; CP, cortical plate; WM, white matter. Scale bar: 50 µm. (E) Quantification of the number of CTIP2$^+$ cells per bin at E14.5. Bin × genotype interaction: $F((9,36) = 9,667$, $p<0.0001$. (F) Quantification of the number of TBR1$^+$ cells per bin at E14.5. Bin × genotype interaction: $F((9,36) = 0,4835$, $p = 0,8760$. (G) Quantification of the number of TBR2$^+$ cells per bin at E14.5. Bin × genotype interaction: $F((9,36) = 0,7968$, $p = 0,6214$. Two-way ANOVA with Bonferroni's post hoc test, ** $p < 0.01$; *** $p < 0.001$; **** $p < 0.0001$. *n* = 3 embryos per genotype.

Fig. 6. Cortical distribution of MEF2C$^+$ and TBR1$^+$ cells at E18 in control and mutant mice.

(A–C') Cortical distribution of MEF2C$^+$ and TBR1$^+$ cells in *Reln*$^{fl/+}$;*Foxg1*$^{Cre/+}$ and *Reln*$^{fl/fl}$;*Foxg1*$^{Cre/+}$ mice at E18. VZ, ventricular zone; IZ, intermediate zone; MZ, marginal zone; I–VI, cortical layers. Scale bar: 50 µm. (D-E) Representative intensity profiles of

MEF2C and TBR1 signal, respectively, plotted as gray value across the cortical wall from layer I to the VZ in control (black) and mutant (red) embryos. (F) Quantification of the number of MEF2C+ cells per bin at E18. In mutant embryos, the MEF2C signal is diffuse across the cortical lamina, with stronger intensity in the marginal zone. Bin × genotype interaction: $F(11, 44) = 7{,}321$ $p<0.0001$; two-way ANOVA with Bonferroni's post hoc test, **** $p < 0.0001$. $n = 3$ embryos per genotype. (E) Quantification of the number of $TBR1^+$ cells per bin at E18. In mutant embryos, the TBR1 signal is shifted superficially, remaining enriched near the marginal zone. Bin × genotype interaction: $F(11, 44) = 58{,}11$ $p<0.0001$; two-way ANOVA with Bonferroni's post hoc test, **** $p < 0.0001$. $n = 3$ embryos per genotype.

Fig. 7. Severe cytoarchitectural disruption of the adult (P30) telencephalon following *Foxg1-Cre*-mediated *reelin* ablation. (A-E') Representative Nissl-stained coronal sections illustrating the mature cytoarchitecture of (A-E) control *Reln*$^{fl/+}$;*Foxg1*$^{Cre/+}$ and (A'-E') mutant *Reln*$^{fl/fl}$;*Foxg1*$^{Cre/+}$ brains at P30. (A-B') High-magnification views of the cerebral and piriform cortices. In the control panel, Roman numerals (I–VI) identify the normal six-layered cortical stratification. (C-E') High-magnification analysis of medial telencephalic and hippocampal structures in (C-E) control *Reln*$^{fl/+}$;*Foxg1*$^{Cre/+}$ and (C'-E') mutant *Reln*$^{fl/fl}$;*Foxg1*$^{Cre/+}$ brains. I–VI, cortical layers; DG, Dentate gyrus; CA1-CA3, Cornu ammonis fields 1 to 3; IG, Indusium griseum; TTd, dorsal taenia tecta; TTv, ventral taenia tecta. n = 3 animals per genotype. Scale bar: 500 μm.

Fig. 8. Severe cortical defects in the late-fetal telencephalon following *Foxg1*-Cre-mediated *reelin* ablation. (A–C) Representative Nissl-stained coronal sections of control *Reln*$^{fl/+}$;*Foxg1*$^{Cre/+}$ and (A'–C') mutant *Reln*^{flfl};*Foxg1*$^{Cre/+}$ brains at E18.5. (A-A') In the isocortex, the black bracket highlights a dense, ectopically displaced cellular band in the mutant cortical plate (CP) compared to the superficial CP of the control. (B-B') In the piriform cortex, lines delineate the three characteristic primitive layers, illustrating a complete loss of laminar organization in the mutant. (C-C') In the hippocampus, Nissl staining does not reveal major differences between control and mutant brains at this developmental stage. (D–F') *In situ* hybridization for *Lpl* mRNA on adjacent sections corroborates the morphological defects. (D-D') In the isocortex, black brackets indicate the *Lpl* expression domain, which is shifted to deeper internal positions in the mutant. (E-E') In the piriform cortex, lines underline *Lpl* expression, revealing a marked reduction and spatial disruption in the mutant. (F-F') In the hippocampus, the asterisk (*) highlights widespread *Lpl* labeling in CA1 of the mutant compared to control. (G–I') *In situ* hybridization for *Lmo3* mRNA. Similar to *Lpl*, (G-G') black brackets indicate a shifted

expression domain in the mutant isocortex. (H-H') In the piriform cortex, *Lmo3* exhibits a mixed expression pattern with a complete loss of layer distinction. (I-I') In the mutant hippocampus, *Lmo3* expression appears abnormally diffuse in the CA1 region (*). (J–J') *In situ* hybridization for *Slit2* mRNA in the hippocampus, showing diffuse expression in the CA1 and dentate gyrus (DG) of the mut*ant* (*). (K–K') *In situ* hybridization for *Zbtb20* mRNA in the hippocampus, highlighting diffuse expression in the mutant DG (*).
*Magnified views in panels (D–I') correspond to regions from the larger overview images presented in Fig. S12 (F, H, F', H' for Lpl; B, D, B', D' for Lmo3).*CA1–3, Cornu Ammonis areas 1–3; cc, corpus callosum; CP, cortical plate; DG, dentate gyrus; ECx, entorhinal cortex; IG, indusium griseum; IZ, intermediate zone; M medial pallium; St, striatum; Sub, subiculum; VZ, ventricular zone. n = 3 embryos per genotype. Scale bar: 500 μm.

Fig. 9. Altered taenia tecta and indusium griseum organization along the rostro-caudal axis in *Reln*$^{fl/fl}$;*Foxg1*$^{Cre/+}$ mutant brains. Representative coronal sections of E18.5 mouse brains showing double immunofluorescence for TBR1 (green) and CTIP2 (red) in the developing taenia tecta (TT) and indusium griseum (IG). Sections were analyzed at three rostro-caudal levels, L1, L2, and L3, corresponding to the section planes indicated by a, b, and d, respectively, in the schematic shown in Fig.S13G. (A–I) Control brains *Reln*$^{fl/+}$;*Foxg1*$^{Cre/+}$; (A′–I′) mutant brains *Reln*$^{fl/fl}$;*Foxg1*$^{Cre/+}$. For each rostro-caudal level, the merged TBR1/CTIP2 signal is shown together with the corresponding individual CTIP2 and TBR1 channels. cc, corpus callosum; IG, indusium griseum; IL, infralimbic cortex; Se, Septum; SCS, subcallosal sling; TT, taenia tecta. n = 3 embryos per genotype. Scale bar: 100 μm.

Fig. 10. Dramatic scattering phenotype in taenia tecta and indusium griseum structures along the rostro-caudal axis at E18.5, **labeled by *Lmo3* and *Zbtb20* expression**. (A-H') Representative coronal sections showing *in situ* hybridization for *Lmo3* and *Zbtb20* in the medial pallium of control (*Reln*$^{fl/+}$;*Foxg1*$^{Cre/+}$) and mutant (*Reln*$^{fl/fl}$;*Foxg1*$^{Cre/+}$) embryos. Four distinct rostro-caudal levels of the developing medial pallium are displayed in columns, corresponding to the section planes indicated by a, b, c and d, respectively, in the schematic shown in Fig.S13G. *Lmo3* expression in the rostro-caudal section of (A–D) *Reln*$^{fl/+}$;*Foxg1*$^{Cre/+}$ control and in (A'-D') *Reln*$^{fl/fl}$;*Foxg1*$^{Cre/+}$ mutant brains. *Zbtb20* expression in the rostro-caudal section of (E–H) *Reln*$^{fl/+}$;*Foxg1*$^{Cre/+}$ control and in (E'-H') *Reln*$^{fl/fl}$;*Foxg1*$^{Cre/+}$ mutant brains. cc, corpus callosum; IG, indusium griseum; IL, infralimbic cortex; LV, lateral ventricle; Se, Septum; SCS, subcallosal sling; TT, taenia tecta; VZ, ventricular zone. n = 3 embryos per genotype. Scale bar: 100 μm.

Fig. 11. *Peg10* and *Lpl* expression confirms the failure of condensation of taenia tecta and indusium griseum along the rostro-caudal axis at E18.5. (A-F') Representative coronal sections showing *in situ* hybridization for *Peg10* and *Lpl* in the medial pallium of control (*Reln*$^{fl/+}$;*Foxg1*$^{Cre/+}$) and mutant (*Reln*$^{fl/fl}$;*Foxg1*$^{Cre/+}$) embryos. Three distinct rostro-caudal levels of the developing medial pallium are displayed in columns, corresponding to the section planes indicated by a, c and d, respectively, in the schematic shown in Fig.S13G. *Peg10* expression in the rostro-caudal section of (A–C) *Reln*$^{fl/+}$;*Foxg1*$^{Cre/+}$ control and in (A'-C') *Reln*$^{fl/fl}$;*Foxg1*$^{Cre/+}$ mutant brains. *Lpl* expression in the rostro-caudal section of (D–F) *Reln*$^{fl/+}$;*Foxg1*$^{Cre/+}$ control and in (D'-F') *Reln*$^{fl/fl}$;*Foxg1*$^{Cre/+}$ mutant brains. cc, corpus callosum; IG, indusium griseum; Se, Septum; TT, taenia tecta; VZ, ventricular zone. n = 3 embryos per genotype. Scale bar: 100 μm.

Fig. 12. Widespread disruption of pallial organization revealed by *Nr4a2* expression. Representative rostro-caudal series of coronal sections showing *Nr4a2* expression in (A–C) control brains (*Reln*$^{fl/+}$;*Foxg1*$^{Cre/+}$) and (A′–C′) mutant brains (*Reln*$^{fl/fl}$;*Foxg1*$^{Cre/+}$) at E18.5. CA1–3, Cornu Ammonis areas 1–3; Clp, claustrum proper; EpD, endopiriform cortex; Hb, habenula; ins, insular cortex; LV, lateral ventricle; Se, septum; SS, somatosensory cortex; Sp, subplate; St, striatum; Sub, subiculum. n = 3 embryos per genotype. Scale bar: 500 μm.

Supplementary figure

Fig. S1. Spatio-temporal pattern of Cre-driven recombination under the control of the *Foxg1* and *Emx1* in the developing telencephalon. YFP reporter expression was visualized using the Rosa26 reporter line (R26R-YFP) at embryonic days E9.5 and E10.5. (A-A'-D-D') Representative whole-mount embryos showing YFP fluorescence images at the indicated developmental stages and in different Cre lines: (A) *Foxg1*$^{Cre/+}$ at E9.5; (A') *Emx1*$^{Cre/+}$ at E9.5; (D) *Foxg1*$^{Cre/+}$ at E10.5; (D') *Emx1*$^{Cre/+}$ at E10.5. (B–B′, E–E′) Representative coronal sections showing the regional distribution of YFP-positive cells in the developing forebrain. (C–C′, F–F′) Higher-magnification views of the regions indicated in B–B′ and E–E′, respectively. Asterisks in C and F in the *Foxg1Cre*$^{/+}$ line indicate YFP-negative cells. n = 3 embryos per Cre line and developmental stage. Di, diencephalon; D, dorsal pallium; E, eye; MB, midbrain; M medial pallium; T, telencephalon; VC, ventricular cavity. Scale bars: 500 μm in A–A′ and D–D′; 100 μm in B–B′, C–C′, E–E′, and F–F′.

Fig. S2. Rostro-caudal distribution of *reelin* mRNA expression in the forebrain following *Foxg1*$^{Cre/+}$ mediated recombination at E12.5. (A-I′) Representative coronal sections from *Reln*$^{fl/+}$;*Foxg1*$^{Cre/+}$ control and *Reln*$^{fl/fl}$;*Foxg1*$^{Cre/+}$ mutant embryos. Three

rostro-caudal levels are shown: L1, A, A′ with corresponding dorsal and ventral magnifications in B, B′ and C, C′, respectively; L2, D, D′ with corresponding dorsal and ventral magnifications in E, E′ and F, F′, respectively; and L3, G, G′ with corresponding dorsal and ventral magnifications in H, H′ and I, I′, respectively. A, amygdala; Cx, cortex; LV, lateral ventricle; M medial pallium; PThE, prethalamic eminence; Se, septum; St, striatum. n = 3 embryos per genotype. Scale bar: 500 µm.

Fig. S3. Rostro-caudal distribution of *reelin* mRNA expression in the forebrain following *Emx1*$^{Cre/+}$ mediated recombination at E12.5. (A–I′) Representative coronal sections from Reln$^{fl/+}$;Emx1$^{Cre/+}$ control and Reln$^{fl/fl}$;Emx1$^{Cre/+}$ mutant embryos. Three rostro-caudal levels are shown: L1, A and A′ with corresponding dorsal and ventral magnifications in B and B′ and C and C′, respectively; L2, D and D′ with corresponding dorsal and ventral magnifications in E and E′ and F and F′, respectively; and L3, G and G′ with corresponding dorsal and ventral magnifications in H and H′ and I and I′, respectively. A, amygdala; Cx, cortex; LV, lateral ventricle; M medial pallium; PThE, prethalamic eminence; Se, septum; St, striatum. n = 3 embryos per genotype. Scale bar: 500 µm.

Fig. S4. Quantification of TBR1$^+$ and TRP73$^+$ cells across the pallium in two conditional *reelin* knockout models. TBR1$^+$ and TRP73$^+$ cells were quantified at three rostro-caudal levels (L1–L3) in *Reln* conditional knockout mice generated using either the *Foxg1*$^{Cre/+}$ and *Emx1*$^{Cre/+}$ driver line. At levels L1 and L2, the pallium was subdivided into four sectors: dorso-medial (DM), dorsal (D), dorso-lateral (DL), and lateral (L). At level L3, the pallium was subdivided into three sectors: dorso-medial (DM), dorso-lateral (DL), and lateral (L). (A, C, E) Quantification of TBR1$^+$ cells in the *Foxg1*$^{Cre/+}$ -mediated *Reln* conditional knockout model at L1, L2, and L3, respectively. (B, D, F) Quantification of TRP73$^+$ cells in the same model at L1, L2, and L3, respectively. (G, I, K) Quantification of TBR1$^+$ cells in the *Emx1*$^{Cre/+}$ -mediated Reln conditional knockout model at L1, L2, and L3, respectively. (H, J, L) Quantification of TRP73$^+$ cells in the same model at L1, L2, and L3, respectively. Data are presented as mean ± SEM. Statistical comparisons were performed using unpaired Student's t-tests. ns, not significant. n = 3 embryos per genotype.

Fig. S5. Immunofluorescence analysis of CALB2 in the dorsal pallium across the rostro-caudal axis at E12.5. (A-L') Representative coronal sections at three rostro-caudal levels (L1, L2, and L3) from control *Reln*$^{fl/+}$*;Foxg1*$^{Cre/+}$ (A-F) and mutant *Reln*$^{fl/fl}$*;Foxg1*$^{Cre/+}$ (A'-F') as well as control *Reln*$^{fl/+}$*;Emx1*$^{Cre/+}$ (G-L) and mutant

Reln$^{fl/fl}$;*Emx1*$^{Cre/+}$ (G'-L') embryos. Boxed areas indicate regions shown at higher magnification. At L1 and L2, the dorsal pallium is subdivided into four anatomical zones: dorso-medial (DM), dorsal (D), dorso-lateral (DL), and lateral (L). At L3, three zones were analyzed (DM, D, DL). n = 3 embryos per genotype. Scale bars: 100 μm.

Fig. S6. Developmental progression of *reelin* mRNA expression in the mouse forebrain. Data from the Allen Developing Mouse Brain Atlas are shown at (A) E11.5, (B) E13.5, (C) E15.5 , and (D) E18.5 , with corresponding higher-magnification views in A′–D′, in which red arrows indicate the CR *Reln*$^{+}$ cells and green arrow *Reln*$^{+}$ GABAergic interneurons. Cx, cortex; St, striatum. Scale bars: 500 μm in A–D and 100 μm in A′–D′.

Fig. S7. Extended rostro-caudal analysis of *reelin* mRNA expression in the *Foxg1*$^{Cre/+}$-mediated *reelin* conditional knockout model. Eight representative coronal sections spanning the rostro-caudal axis are shown at E14.5, arranged from rostral to caudal. (A–H) Sections from *Reln*$^{fl/+}$;*Foxg1*$^{Cre/+}$ control brains and (A′–H′) corresponding sections from *Reln*$^{fl/fl}$;*Foxg1*$^{Cre/+}$ mutant brains, analyzed by *in situ* hybridization for *Reln* mRNA. Black arrows indicate few residual *Reln*+ cells. Cx, cortex; Hb, habenula; Hi, hippocampus; M medial pallium; Pal, pallium; PT, Pretectum; PThE, prethalamic eminence; Se, septum; St, striatum; Th, thalamus. n = 3 embryos per genotype. Scale bar, 500 μm.

Fig. S8. *reelin* mRNA expression and comparative cytoarchitectural analysis of *Foxg1*$^{Cre/+}$ and *Emx1*$^{Cre/+}$ mediated *reelin* cKO mutants at E18.5. (A–C) Representative coronal sections from a wild-type (WT) embryo at E18.5, showing the normal spatial distribution of *Reln* mRNA in the developing forebrain across the rostro-caudal axis, detected by *ISH*. (D–I′) Representative Nissl-stained coronal sections from control embryos and *Reln* conditional mutants at three rostro-caudal levels. (D–F) *Reln*$^{fl/+}$;*Foxg1*$^{Cre/+}$ control sections. (D′–F′) Sections from *Reln*$^{fl/fl}$;*Foxg1*$^{Cre/+}$ mutant embryos. (G–I) *Reln*$^{fl/+}$;*Emx1*$^{Cre/+}$ control sections and (G′–I′) sections from *Reln*$^{fl/fl}$;*Emx1*$^{Cre/+}$ mutant embryos. CA1–3, cornu Ammonis areas 1–3; CP, cortical plate; DG, dentate gyrus; Pir, piriform cortex; Se, septum; St, striatum. n = 3 embryos per genotype. Scale bar: 500 μm.

Fig. S9. Extended rostro-caudal analysis of *reelin* mRNA expression in the *Foxg1*$^{Cre/+}$-mediated *reelin* conditional knockout model. Ten representative coronal sections spanning the rostro-caudal axis are shown at E18.5, arranged from rostral to

caudal. (A–J) Sections from *Reln*$^{fl/+}$;*Foxg1*$^{Cre/+}$ control brains and (A′–J′) corresponding sections from *Reln*$^{fl/fl}$;*Foxg1*$^{Cre/+}$ mutant brains, analyzed by *in situ* hybridization for *Reln* mRNA. Cx, cortex; Hb, habenula; Hi, hippocampus; M medial pallium; Se, septum; St, striatum. n = 3 embryos per genotype. Scale bar, 500 µm.

Fig. S10. Cortical distribution of MEF2C$^+$ and TBR1$^+$ cells at E18.5 in control and mutant mice. (A–C') Cortical distribution of MEF2C$^+$ and TBR1$^+$ cells in *Reln*$^{fl/+}$;*Emx1*$^{Cre/+}$ and *Reln*$^{fl/fl}$;*Emx1*$^{Cre/+}$ mice at E18.5. VZ, ventricular zone; IZ, intermediate zone; MZ, marginal zone; I–VI, cortical layers. Scale bar: 50 µm. (D-E) Representative intensity profiles of MEF2C and TBR1 signal, respectively, plotted as gray value across the cortical wall from layer I to the VZ in control (black) and mutant (blue) embryos. (F) Quantification of the number of MEF2C+ cells per bin at E18.5. In mutant embryos, the MEF2C signal is diffuse across the cortical lamina, with stronger intensity in the marginal zone. Bin × genotype interaction: F(11, 24) = 0,6525 p = 0,7611; two-way ANOVA with Bonferroni's post hoc test. *n* = 3 embryos per genotype. (E) Quantification of the number of TBR1$^+$ cells per bin at E18.5. In mutant embryos, the TBR1 signal is shifted superficially, remaining enriched near the marginal zone. Bin × genotype interaction: F(11, 24) = 2,105 p=0.0618; two-way ANOVA with Bonferroni's post hoc test, *p<0.05; **p<0.01. *n* = 3 embryos per genotype.

Fig. S11. Preserved telencephalic cytoarchitecture in P30 mice following pallium-restricted *Emx1-Cre*-mediated *reelin* ablation. (A-E') Representative Nissl-stained coronal sections illustrating the mature cytoarchitecture of (A-E) control *Reln*$^{fl/+}$;*Emx1*$^{Cre/+}$ and (A'-E') mutant *Reln*$^{fl/fl}$;*Emx1*$^{Cre/+}$ brains at P30. (A-B') High-magnification views of the cerebral and piriform cortices. In the control panel, Roman numerals (I–VI) identify the normal six-layered cortical stratification. (C-E') High-magnification analysis of medial telencephalic and hippocampal structures in (C-E) control *Reln*$^{fl/+}$;*Emx1*$^{Cre/+}$ and (C'-E') mutant *Reln*$^{fl/fl}$;*Emx1*$^{Cre/+}$ brains.CA1–CA3, cornu Ammonis fields 1–3; DG, dentate gyrus; IG, indusium griseum; TTd, dorsal taenia tecta; TTv, ventral taenia tecta. n = 3 animals per genotype. Scale bar: 500 µm.

Fig. S12. Rostro-caudal expression patterns of *Lmo3* and *Lpl* mRNAs in control and mutant forebrains. Four representative coronal sections spanning the rostro-caudal axis are shown at E18.5 control embryos (*Reln*$^{fl/+}$;*Foxg1*$^{Cre/+}$) and mutant embryos (*Reln*$^{fl/fl}$;*Foxg1*$^{Cre/+}$), arranged from rostral to caudal. *Lmo3* mRNA expression, analyzed by *in situ* hybridization, in (A–D) control and (A′–D′) mutant sections. (E–H and E′–H′) *Lpl* mRNA expression in (E–H) the control and (E′–H′) mutant sections. The low-magnification

sections shown here correspond to the higher-magnification views presented in Fig. 8 D-I'. In panel A', *TT* indicates the expected anatomical position of the taenia tecta, where the expected *Lmo3* labeling is absent. cc, corpus callosum; CP, cortical plate; Cx, cortex; Hi, hippocampus; IG, indusium griseum; M medial pallium; Pir, piriform cortex; Se, septum; St, striatum; Sub, subiculum; TT, taenia tecta. n = 3 embryos per genotype. Scale bar, 500 μm.

Fig. S13. Sagittal expression patterns of *Peg10* and *Zbtb20* in the E18.5 mouse telencephalon. Representative *in situ* hybridization images obtained from the Allen Developing Mouse Brain Atlas are shown in sagittal sections. (A–C) *Peg10* mRNA expression delineates the taenia tecta (TT) and indusium griseum (IG), with corresponding higher-magnification views in B′ and C′. (D–F) *Zbtb20* mRNA expression is similarly detected in the TT and IG, with corresponding higher-magnification views in E′ and F′. (G) Schematic representation of the TT, IG, corpus callosum (cc), and hippocampus (Hi), indicating the sagittal section planes corresponding to the regions shown in the main Figures 9–11. ac, anterior commissure; CA1, cornu Ammonis area 1; Cb, cerebellum; cc, corpus callosum; Cx, cortex; fx, fornix; Hb, habenula; hc, hippocampal commissure; Hi, hippocampus; IG, indusium griseum; MB, midbrain; PC, posterior commissure; PG, pineal gland; PTh, prethalamus; PT, pretectum; rf, rhinal fissure; Rh, rhombencephalon; Se, septum; St, striatum; Th, thalamus; TT, taenia tecta. Scale bar: 500 μm.

Fig. S14. Extended rostro-caudal analysis of pallial organization revealed by *Nr4a2* expression. Representative series of ten coronal sections spanning the rostro-caudal axis of (A–J) control brains (*Reln*$^{fl/+}$;*Foxg1*$^{Cre/+}$) and (A′–J′) mutant brains (*Reln*$^{fl/fl}$;*Foxg1*$^{Cre/+}$) at E18.5, showing *Nr4a2* expression by *in situ* hybridization. The ten rostro-caudal levels shown here provide an extended view of the pallial abnormalities observed in the representative sections presented in main Fig. 12. CA1–3, Cornu Ammonis areas 1–3; Clp, claustrum proper; EpD, endopiriform cortex; Hb, habenula; ins, insular cortex; LV, lateral ventricle; Se, septum; SS, somatosensory cortex; Sp, subplate; St, striatum; Sub, subiculum. n = 3 embryos per genotype. Scale bar: 500 μm.

Bibliography

Alcántara, S., Ruiz, M., D'Arcangelo, G., Ezan, F., De Lecea, L., Curran, T., Sotelo, C., & Soriano, E. (1998). Regional and cellular patterns of reelin mRNA expression in the forebrain of the developing and adult mouse. *Journal of Neuroscience*, *18*(19), 7779–7799. https://doi.org/10.1523/jneurosci.18-19-07779.1998

Angevine, J. B., & Sidman, R. L. (1961). Autoradiographic Study of Cell Migration during Histogenesis of Cerebral Cortex in the Mouse. *Nature*, *192*(4804), 766–768. https://doi.org/10.1038/192766b0

Arcangelo, G. D., & Curran, T. (1998). *Reeler : new tales on an old mutant mouse*. 235–244. https://doi.org/10.1002/(SICI)1521-1878(199803)20

Barber, M., & Pierani, A. (2016). Tangential migration of glutamatergic neurons and cortical patterning during development: Lessons from Cajal-Retzius cells. *Developmental Neurobiology*, *76*(8), 847–881. https://doi.org/10.1002/dneu.22363

Bielle, F., Griveau, A., Narboux-Nême, N., Vigneau, S., Sigrist, M., Arber, S., Wassef, M., & Pierani, A. (2005). Multiple origins of Cajal-Retzius cells at the borders of the developing pallium. *Nature Neuroscience*, *8*(8), 1002–1012. https://doi.org/10.1038/nn1511

Blume, M., Inoguchi, F., Sugiyama, T., Owada, Y., Osumi, N., Aimi, Y., Taki, K., & Katsuyama, Y. (2017). *Dab1 contributes differently to the morphogenesis of the hippocampal subdivisions*. 657–673. https://doi.org/10.1111/dgd.12393

Boyle, M. P., Bernard, A., Thompson, C. L., Ng, L., Boe, A., Mortrud, M., Hawrylycz, M. J., Jones, A. R., Hevner, R. F., & Lein, E. S. (2011). Cell-type-specific consequences of reelin deficiency in the mouse neocortex, hippocampus, and amygdala. *Journal of Comparative Neurology*, *519*(11), 2061–2089. https://doi.org/10.1002/cne.22655

Briata, P., Di Blas, E., Gulisano, M., Mallamaci, A., Iannone, R., Boncinelli, E., & Corte, G. (1996). EMX1 homeoprotein is expressed in cell nuclei of the developing cerebral cortex and in the axons of the olfactory sensory neurons. *Mechanisms of Development*, *57*(2), 169–180. https://doi.org/10.1016/0925-4773(96)00544-8

Bruguier, H., Suarez, R., Manger, P., Hoerder-suabedissen, A., Shelton, A. M., Packer, A. M., Ferran, J. L., Puelles, L., Molnár, Z., & Oliver, D. K. (2020). *In search of common developmental and evolutionary origin of the claustrum and subplate*. *January*, 2956–2977. https://doi.org/10.1002/cne.24922

Cadwell, C. R., Bhaduri, A., Mostajo-Radji, M. A., Keefe, M. G., & Nowakowski, T. J. (2019). Development and Arealization of the Cerebral Cortex. *Neuron*, *103*(6), 980–1004. https://doi.org/10.1016/j.neuron.2019.07.009

Causeret, F., Moreau, M. X., Pierani, A., & Blanquie, O. (2021). The multiple facets of Cajal-Retzius neurons. *Development (Cambridge)*, *148*(11). https://doi.org/10.1242/DEV.199409

Caviness, V. S. (1982). Neocortical histogenesis in normal and reeler mice: A developmental study based upon [3H]thymidine autoradiography. *Developmental Brain Research*, *4*(3), 293–302. https://doi.org/10.1016/0165-3806(82)90141-9

Cionni, M., Menke, C., & Stottmann, R. W. (2016). Novel genetic tools facilitate the study of cortical neuron migration. *Mammalian Genome*, *27*(1–2), 8–16. https://doi.org/10.1007/s00335-015-9615-6

Cooper, J. A. (2008). *A mechanism for inside-out lamination in the neocortex*. *February*,

113–119. https://doi.org/10.1016/j.tins.2007.12.003
D'Arcangelo, G., G. Miao, G., Chen, S.-C., Scares, H. D., Morgan, J. I., & Curran, T. (1995). A protein related to extracellular matrix proteins deleted in the mouse mutant reeler. *Nature*, *374*(6524), 719–723. https://doi.org/10.1038/374719a0
de Frutos, C. A., Bouvier, G., Arai, Y., Thion, M. S., Lokmane, L., Keita, M., Garcia-Dominguez, M., Charnay, P., Hirata, T., Riethmacher, D., Grove, E. A., Tissir, F., Casado, M., Pierani, A., & Garel, S. (2016). Reallocation of Olfactory Cajal-Retzius Cells Shapes Neocortex Architecture. *Neuron*, *92*(2), 435–448. https://doi.org/10.1016/j.neuron.2016.09.020
Di Ieva, A., Fathalla, H., Cusimano, M. D., & Tschabitscher, M. (2015). The indusium griseum and the longitudinal striae of the corpus callosum. *Cortex; a Journal Devoted to the Study of the Nervous System and Behavior*, *62*, 34–40. https://doi.org/10.1016/j.cortex.2014.06.016
Dulabon, L., Olson, E. C., Taglienti, M. G., Eisenhuth, S., McGrath, B., Walsh, C. A., Kreidberg, J. A., & Anton, E. S. (2000). Reelin Binds α3β1 Integrin and Inhibits Neuronal Migration. *Neuron*, *27*(1), 33–44. https://doi.org/10.1016/S0896-6273(00)00007-6
Elorriaga, V., Bouloudi, B., Delberghe, E., Saillour, Y., Morel, J. S., Azzam, P., Moreau, M. X., Stottmann, R., Bahi-Buisson, N., Pierani, A., Spassky, N., & Causeret, F. (2025). Differential contribution of P73+ Cajal-Retzius cells and Reelin to cortical morphogenesis. *Development*, *152*(9), dev204451. https://doi.org/10.1242/dev.204451
Elorriaga, V., Pierani, A., & Causeret, F. (2023). Cajal-retzius cells: Recent advances in identity and function. *Current Opinion in Neurobiology*, *79*(April), 1–8. https://doi.org/10.1016/j.conb.2023.102686
Farley, F. W., Soriano, P., Steffen, L. S., & Dymecki, S. M. (2000). *Widespread Recombinase Expression Using FLPeR (Flipper) Mice*. *110*, 106–110.
Franco, S. J., & Müller, U. (2013). Shaping Our Minds: Stem and Progenitor Cell Diversity in the Mammalian Neocortex. *Neuron*, *77*(1), 19–34. https://doi.org/10.1016/j.neuron.2012.12.022
Frotscher, M., Haas, C. A., Förster, E., Institut, A., & Freiburg, U. (2003). *Reelin Controls Granule Cell Migration in the Dentate Gyrus by Acting on the Radial Glial Scaffold*. 634–640.
García-Cabezas, M. Á., Hacker, J. L., & Zikopoulos, B. (2023). Homology of neocortical areas in rats and primates based on cortical type analysis: an update of the Hypothesis on the Dual Origin of the Neocortex. *Brain Structure & Function*, *228*(5), 1069–1093. https://doi.org/10.1007/s00429-022-02548-0
Gil, V., Nocentini, S., Del Rio, J. A., & del Río, J. A. (2014). Historical first descriptions of Cajal-Retzius cells: from pioneer studies to current knowledge. *Front Neuroanat*, *8*(MAY), 32. https://doi.org/10.3389/fnana.2014.00032
Gilmore, E. C., & Herrup, K. (2000). Cortical development: Receiving Reelin. *Current Biology*, *10*(4), R162–R166. https://doi.org/10.1016/S0960-9822(00)00332-8
Gorski, J. A., Talley, T., Qiu, M., Puelles, L., Rubenstein, J. L. R., & Jones, K. R. (2002). Cortical excitatory neurons and glia, but not GABAergic neurons, are produced in the Emx1-expressing lineage. *Journal of Neuroscience*, *22*(15), 6309–6314. https://doi.org/10.1523/jneurosci.22-15-06309.2002

Götz, M., & Huttner, W. B. (2005). The cell biology of neurogenesis. *Nature Reviews. Molecular Cell Biology*, *6*(10), 777–788. https://doi.org/10.1038/nrm1739

Griveau, A., Borello, U., Causeret, F., Tissir, F., Boggetto, N., Karaz, S., & Pierani, A. (2010). A Novel Role for Dbx1-Derived Cajal-Retzius Cells in Early Regionalization of the Cerebral Cortical Neuroepithelium. *PLoS Biology*, *8*(7), e1000440. https://doi.org/10.1371/journal.pbio.1000440

Gulisano, M., Broccoli, V., Pardini, C., & Boncinelli, E. (1996). *Emx1* and *Emx2* Show Different Patterns of Expression During Proliferation and Differentiation of the Developing Cerebral Cortex in the Mouse. *European Journal of Neuroscience*, *8*(5), 1037–1050. https://doi.org/10.1111/j.1460-9568.1996.tb01590.x

Hack, I., Hellwig, S., Junghans, D., Brunne, B., Bock, H. H., Zhao, S., & Frotscher, M. (2007). *Divergent roles of ApoER2 and Vldlr in the migration of cortical neurons*. *3891*, 3883–3891. https://doi.org/10.1242/dev.005447

Hanashima, C., Fernandes, M., Hebert, J. M., & Fishell, G. (2007). The role of Foxg1 and dorsal midline signaling in the generation of Cajal-Retzius subtypes. *J Neurosci*, *27*(41), 11103–11111. https://doi.org/10.1523/JNEUROSCI.1066-07.2007

Hanashima, C., Li, S. C., Shen, L., Lai, E., & Fishell, G. (2004). Foxg1 suppresses early cortical cell fate. *Science (New York, N.Y.)*, *303*(5654), 56–59. https://doi.org/10.1126/science.1090674

Hébert, J. M., & McConnell, S. K. (2000). Targeting of cre to the Foxg1 (BF-1) Locus Mediates loxP Recombination in the Telencephalon and Other Developing Head Structures. *Developmental Biology*, *222*(2), 296–306. https://doi.org/10.1006/dbio.2000.9732

Hevner, R. F., Daza, R. A., Rubenstein, J. L., Stunnenberg, H., Olavarria, J. F., & Englund, C. (2003). Beyond laminar fate: toward a molecular classification of cortical projection/pyramidal neurons. *Dev Neurosci*, *25*(2–4), 139–151. https://doi.org/10.1159/000072263 DNE20030252_4139 [pii]

Hevner, R. F., Shi, L., Justice, N., Hsueh, Y., Sheng, M., Smiga, S., Bulfone, A., Goffinet, M., Campagnoni, A. T., Rubenstein, J. L. R., Ireland, N., & Hughes, H. (2001). *Tbr1 Regulates Differentiation of the Preplate and Layer 6*. *29*, 353–366.

Jossin, Y. (2004). Neuronal Migration and the Role of Reelin During Early Development of the Cerebral Cortex. *Molecular Neurobiology*, *30*(3), 225–252. https://doi.org/10.1385/MN:30:3:225

Jossin, Y., Ogawa, M., Metin, C., & Tissir, F. (2003). *Inhibition of Src Family Kinases and Non-Classical Protein Kinases C Induce a Reeler-Like Malformation of Cortical Plate Development*. *23*(30), 9953–9959.

Katsuyama, Y., & Terashima, T. (2009). Developmental anatomy of *reeler* mutant mouse. *Development, Growth & Differentiation*, *51*(3), 271–286. https://doi.org/10.1111/j.1440-169X.2009.01102.x

Kelsom, C., & Lu, W. (2013). Development and specification of GABAergic cortical interneurons. *Cell & Bioscience*, *3*(1), 19. https://doi.org/10.1186/2045-3701-3-19

Kessaris, N., Fogarty, M., Iannarelli, P., Grist, M., Wegner, M., & Richardson, W. D. (2006). Competing waves of oligodendrocytes in the forebrain and postnatal elimination of an embryonic lineage. *Nature Neuroscience*, *9*(2), 173–179.

https://doi.org/10.1038/nn1620
Kikkawa, T., Sakayori, N., Yuuki, H., Katsuyama, Y., Matsuzaki, F., Konno, D., Abe, T., Kiyonari, H., & Osumi, N. (2020). Dmrt genes participate in the development of Cajal-Retzius cells derived from the cortical hem in the telencephalon. *Developmental Dynamics : An Official Publication of the American Association of Anatomists*, *249*(6), 698–710. https://doi.org/10.1002/dvdy.156
Kubo, K., Honda, T., Tomita, K., Sekine, K., Ishii, K., Uto, A., Kobayashi, K., Tabata, H., & Nakajima, K. (2010). Ectopic Reelin induces neuronal aggregation with a normal birthdate-dependent "inside-out" alignment in the developing neocortex. *The Journal of Neuroscience : The Official Journal of the Society for Neuroscience*, *30*(33), 10953–10966. https://doi.org/10.1523/JNEUROSCI.0486-10.2010
Kumamoto, T., Toma, K., Gunadi, McKenna, W. L., Kasukawa, T., Katzman, S., Chen, B., & Hanashima, C. (2013). Foxg1 coordinates the switch from nonradially to radially migrating glutamatergic subtypes in the neocortex through spatiotemporal repression. *Cell Rep*, *3*(3), 931–945. https://doi.org/10.1016/j.celrep.2013.02.023
Lane-Donovan, C., Philips, G. T., Wasser, C. R., Durakoglugil, M. S., Masiulis, I., Upadhaya, A., Pohlkamp, T., Coskun, C., Kotti, T., Steller, L., Hammer, R. E., Frotscher, M., Bock, H. H., & Herz, J. (2015). Reelin protects against amyloid β toxicity in vivo. *Science Signaling*, *8*(384). https://doi.org/10.1126/scisignal.aaa6674
Liu, B., Xiao, H., & Zhao, C. (2018). Forced Expression of Foxg1 in the Cortical Hem Leads to the Transformation of Cajal-Retzius Cells into Dentate Granule Neurons. *Journal of Developmental Biology*, *6*(3), 16. https://doi.org/10.3390/jdb6030016
Lucero-Arteaga, F., Labegorra, S., Abrego-Alvarez, A., Heck, V., Portu, A. I., Boeris, M. A., Alonso, A., Do-Couto, B. R., García-Cabezas, M. Á., Tseng, K. Y., & Ferran, J. L. (2025). Elucidating the neuromeric organization of the Mongolian gerbil brain. *Brain Structure and Function*, *230*(8). https://doi.org/10.1007/s00429-025-03018-z
Lucero-Arteaga, F., Abrego-Alvarez, A., Clauzure, M., Labegorra, S., Heck, V., Portu, A. I., Boeris, M. A., Mondino, M. A., Do-Couto, B. R., Tseng, K. Y., García-Cabezas, M. Á., & Ferran, J. L. (2026). Neuromeric Organization of the Microbat Brain: Conserved and Distinct Regional Features. *Journal of Comparative Neurology*, *534*(2). https://doi.org/10.1002/cne.70140
Magno, L., Asgarian, Z., Apanaviciute, M., Milner, Y., Bengoa-Vergniory, N., Rubin, A. N., & Kessaris, N. (2022). Fate mapping reveals mixed embryonic origin and unique developmental codes of mouse forebrain septal neurons. *Communications Biology*, *5*(1), 1–15. https://doi.org/10.1038/s42003-022-04066-5
Martínez-Cerdeño, V., & Noctor, S. C. (2014). Cajal, Retzius, and Cajal-Retzius cells. *Frontiers in Neuroanatomy*, *8*(JUN), 1–7. https://doi.org/10.3389/fnana.2014.00048
Meyer, G. (2010). *Building a human cortex: the evolutionary differentiation of Cajal-Retzius cells and the cortical hem*. 334–343. https://doi.org/10.1111/j.1469-7580.2010.01266.x
Meyer, G., Cabrera Socorro, A., Perez Garcia, C. G., Martinez Millan, L., Walker, N., & Caput, D. (2004). Developmental roles of p73 in Cajal-Retzius cells and cortical patterning. *J Neurosci*, *24*(44), 9878–9887. https://doi.org/10.1523/JNEUROSCI.3060-04.2004
Mingo-moreno, N., Truschow, P., Staiger, J. F., & Wagener, R. J. (2024). *Caudally pronounced deficiencies in preplate splitting and migration underly a rostro-caudal*

progression of cortical lamination defects in the reeler brain. *February*.
Muzio, L., & Mallamaci, A. (2005). Foxg1 confines Cajal-Retzius neuronogenesis and hippocampal morphogenesis to the dorsomedial pallium. *J Neurosci*, *25*(17), 4435–4441. http://www.ncbi.nlm.nih.gov/entrez/query.fcgi?cmd=Retrieve&db=PubMed&dopt=Citation&list_uids=15858069
Ogawa, M., Miyata, T., Nakajimat, K., Yagyu, K., Seike, M., Ikenaka, K., Yamamoto, H., & Mikoshibat, K. (1995). The reeler gene-associated antigen on cajal-retzius neurons is a crucial molecule for laminar organization of cortical neurons. *Neuron*, *14*(5), 899–912. https://doi.org/10.1016/0896-6273(95)90329-1
Oshima, K., Yoshinaga, S., Kitazawa, A., Hirota, Y., & Kubo, K. (2023). *A Unique " Reversed " Migration of Neurons in the Developing Claustrum*. *43*(5), 693–708.
Pahle, J., Muhia, M., Wagener, R. J., Tippmann, A., Bock, H. H., Graw, J., Herz, J., Staiger, J. F., Drakew, A., Kneussel, M., Rune, G. M., Frotscher, M., & Brunne, B. (2019). Selective Inactivation of Reelin in Inhibitory Interneurons Leads to Subtle Changes in the Dentate Gyrus But Leaves Cortical Layering and Behavior Unaffected. *Cerebral Cortex*, *30*(3), 1688–1707. https://doi.org/10.1093/cercor/bhz196
Parnavelas, J. G. (2000). The origin and migration of cortical neurones: new vistas. *Trends in Neurosciences*, *23*(3), 126–131. https://doi.org/10.1016/S0166-2236(00)01553-8
Puelles, L. (2014). *Chapter 4 - Development and Evolution of the Claustrum* (J. R. Smythies, L. R. Edelstein, & V. S. B. T.-T. C. Ramachandran (eds.); pp. 119–176). Academic Press. https://doi.org/https://doi.org/10.1016/B978-0-12-404566-8.00004-0
Puelles, L. (2017). *Comments on the Updated Tetrapartite Pallium Model in the Mouse and Chick , Featuring a Homologous Claustro-Insular Complex*. *2017*, 171–189. https://doi.org/10.1159/000479782
Puelles, L., Ayad, A., Alonso, A., Sandoval, J. E., Mart, M., Medina, L., & Ferran, J. L. (2016). *Selective Early Expression of the Orphan Nuclear Receptor Nr4a2 Identifies the Claustrum Homolog in the Avian Mesopallium : Impact on Sauropsidian / Mammalian Pallium Comparisons*. *703*, 665–703. https://doi.org/10.1002/cne.23902
Puelles, L., & García-calero, E. (2024). *Genoarchitectural Definition of the Adult Mouse Mesocortical Ring : A Contribution to Cortical Ring Theory*. https://doi.org/10.1002/cne.25647
Puelles, L., Kuwana, E., Puelles, E., Bulfone, A., Shimamura, K., Keleher, J., Smiga, S., & Rubenstein, J. L. (2000). Pallial and subpallial derivatives in the embryonic chick and mouse telencephalon, traced by the expression of the genes Dlx-2, Emx-1, Nkx-2.1, Pax-6, and Tbr-1. *The Journal of Comparative Neurology*, *424*(3), 409–438. https://doi.org/10.1002/1096-9861(20000828)424:3<409::aid-cne3>3.0.co;2-7
Puelles, L., & Rubenstein, J. L. R. (2003). Forebrain gene expression domains and the evolving prosomeric model. *Trends in Neurosciences*, *26*(9), 469–476. https://doi.org/10.1016/S0166-2236(03)00234-0
Puelles, L., & Rubenstein, J. L. R. (2015). A new scenario of hypothalamic organization: rationale of new hypotheses introduced in the updated prosomeric model. *Frontiers*

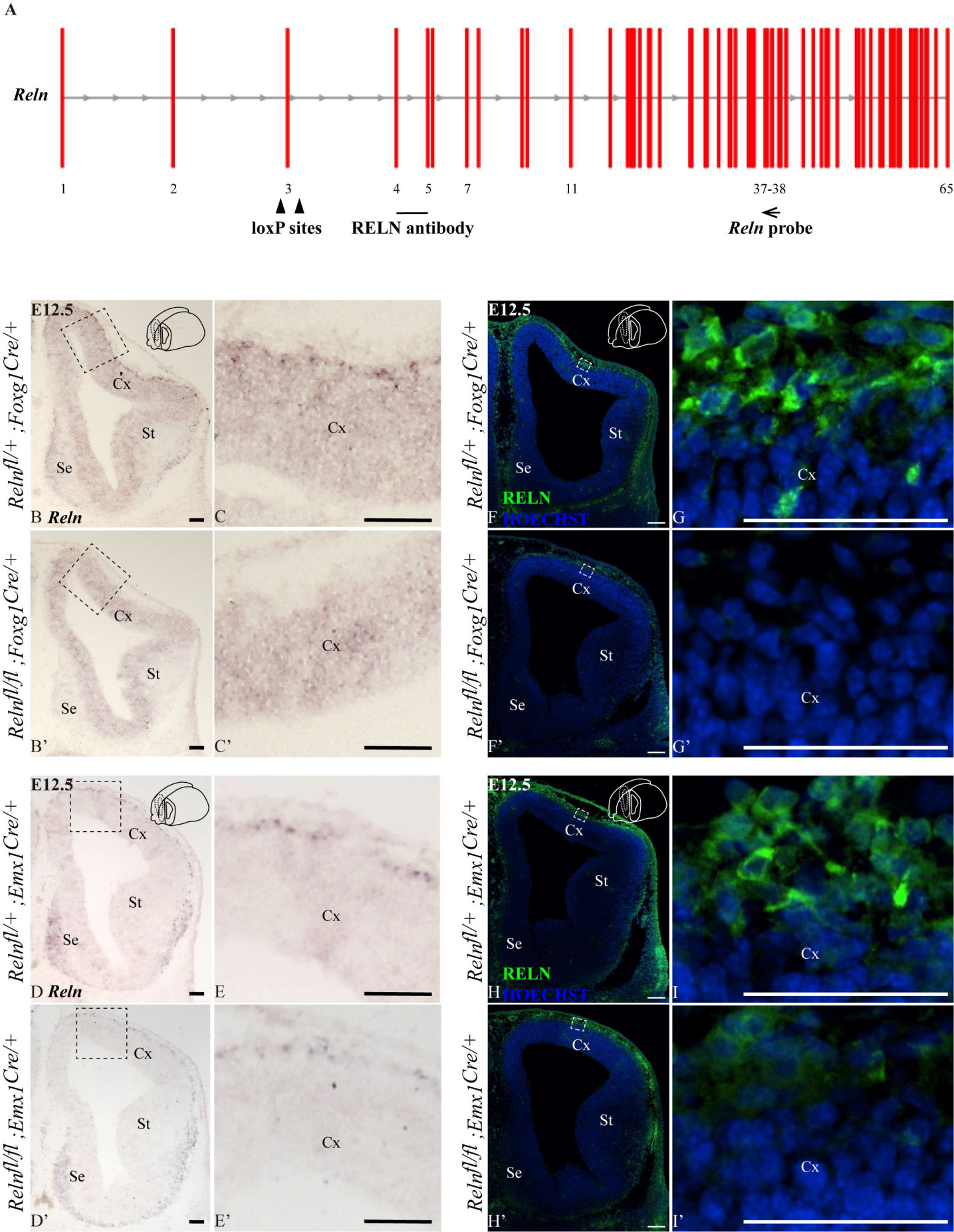
in Neuroanatomy, *9*. https://doi.org/10.3389/fnana.2015.00027
Ruiz-Reig, N., Andrés, B., Huilgol, D., Grove, E. A., Tissir, F., Tole, S., Theil, T., Herrera, E., & Fairén, A. (2016). Lateral Thalamic Eminence: A Novel Origin for mGluR1/Lot Cells. *Cerebral Cortex*, bhw126. https://doi.org/10.1093/cercor/bhw126
Ruiz-Reig, N., & Studer, M. (2017). Rostro-Caudal and Caudo-Rostral Migrations in the Telencephalon: Going Forward or Backward? *Frontiers in Neuroscience*, *11*. https://doi.org/10.3389/fnins.2017.00692
Sanides, F. (1962). Einführung. In *Monographien aus dem Gesamtgebiete der Neurologie und Psychiatrie* (pp. 1–7). https://doi.org/10.1007/978-3-642-86210-6_1
Schneider-lódi, M., Ahrari, A., Meseke, M., Corvace, F., Kümmel, M., Trampe, A., Hamad, M. I. K., & Förster, E. (2025). *Early Postnatally Induced Conditional Reelin Deficiency Causes Malformations of Hippocampal Neurons*. 1–17.
Sekine, K., Honda, T., Kawauchi, T., Kubo, K., & Nakajima, K. (2011). *The Outermost Region of the Developing Cortical Plate Is Crucial for Both the Switch of the Radial Migration Mode and the Dab1-Dependent " Inside-Out " Lamination in the Neocortex*. *31*(25), 9426–9439. https://doi.org/10.1523/JNEUROSCI.0650-11.2011
Sibbe, M., Fo, E., Basak, O., Taylor, V., & Frotscher, M. (2009). *Reelin and Notch1 Cooperate in the Development of the Dentate Gyrus*. *29*(26), 8578–8585. https://doi.org/10.1523/JNEUROSCI.0958-09.2009
Simeone, A., Acampora, D., Gulisano, M., Stornaiuolo, A., & Boncinelli, E. (1992). Nested expression domains of four homeobox genes in developing rostral brain. *Nature*, *358*(6388), 687–690. https://doi.org/10.1038/358687a0
Soriano, E., & Del Rio, J. A. (2005). The cells of cajal-retzius: still a mystery one century after. *Neuron*, *46*(3), 389–394. https://doi.org/S0896-6273(05)00355-7 [pii] 10.1016/j.neuron.2005.04.019
Soriano, P. (1999). *Generalized lacZ expression with the ROSA26 Cre reporter strain*. *21*(january), 70–71.
Srinivas, S., Watanabe, T., Lin, C.-S., William, C. M., Tanabe, Y., Jessell, T. M., & Costantini, F. (2001). Cre reporter strains produced by targeted insertion of EYFP and ECFP into the ROSA26 locus. *BMC Developmental Biology*, *1*(1). https://doi.org/10.1186/1471-213X-1-4
Supèr, H., Martínez, A., Del Río, J. A., & Soriano, E. (1998). Involvement of Distinct Pioneer Neurons in the Formation of Layer-Specific Connections in the Hippocampus. *The Journal of Neuroscience*, *18*(12), 4616–4626. https://doi.org/10.1523/jneurosci.18-12-04616.1998
Tissir, F., Ravni, A., Achouri, Y., Riethmacher, D., Meyer, G., & Goffinet, A. M. (2009). DeltaNp73 regulates neuronal survival in vivo. *Proceedings of the National Academy of Sciences*, *106*(39), 16871–16876. https://doi.org/10.1073/pnas.0903191106
Vilchez-Acosta, A., Manso, Y., Cardenas, A., Elias-Tersa, A., Martinez-Losa, M., Pascual, M., Alvarez-Dolado, M., Nairn, A. C., Borrell, V., & Soriano, E. (2022). Specific contribution of Reelin expressed by Cajal-Retzius cells or GABAergic interneurons to cortical lamination. *Proceedings of the National Academy of Sciences of the United States of America*, *119*(37), 1–25. https://doi.org/10.1073/pnas.2120079119
Xuan, S., Baptista, C. A., Balas, G., Tao, W., Soares, V. C., & Lai, E. (1995). Winged

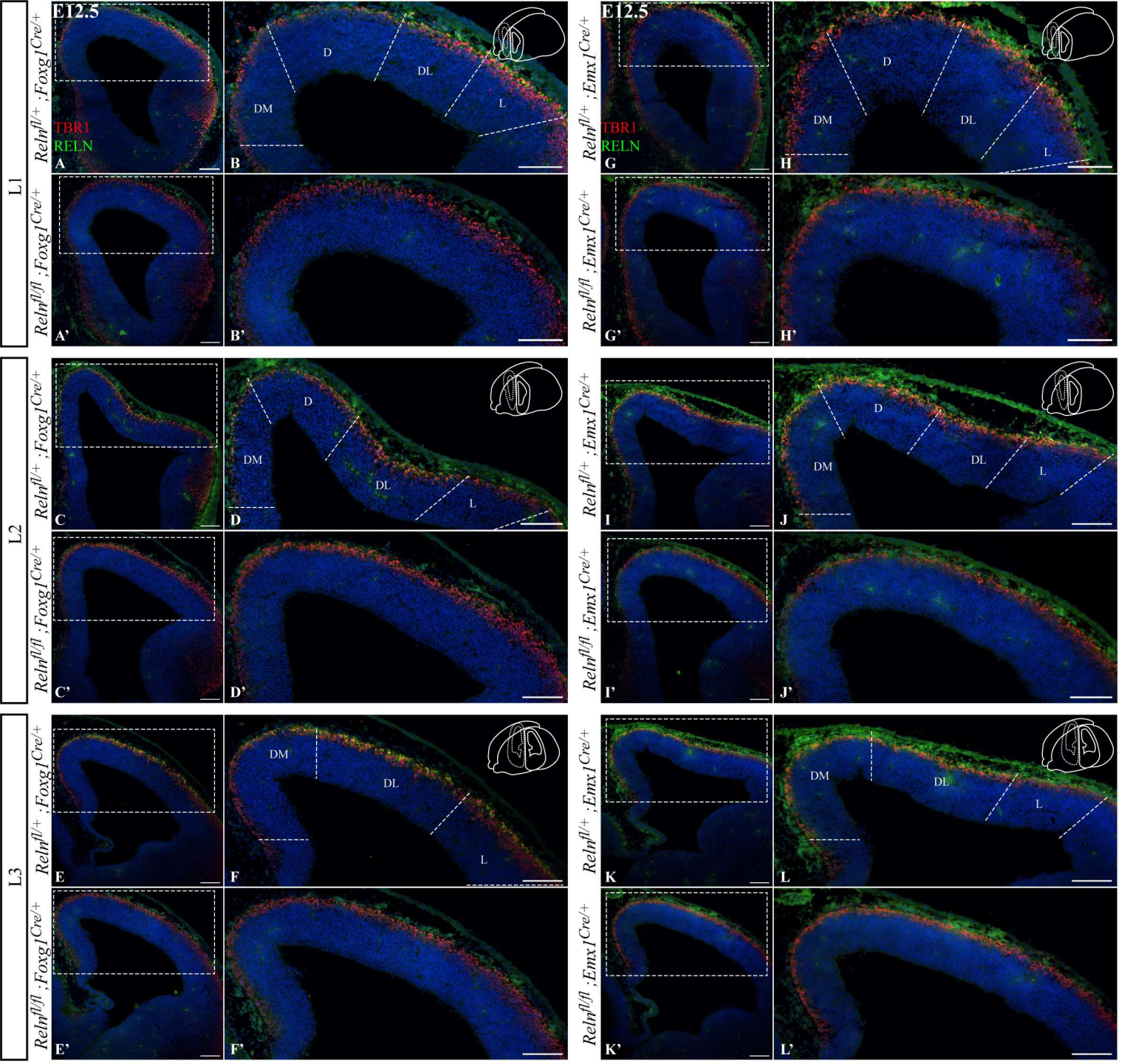
helix transcription factor BF-1 is essential for the development of the cerebral hemispheres. *Neuron*, *14*(6), 1141–1152. https://doi.org/10.1016/0896-6273(95)90262-7

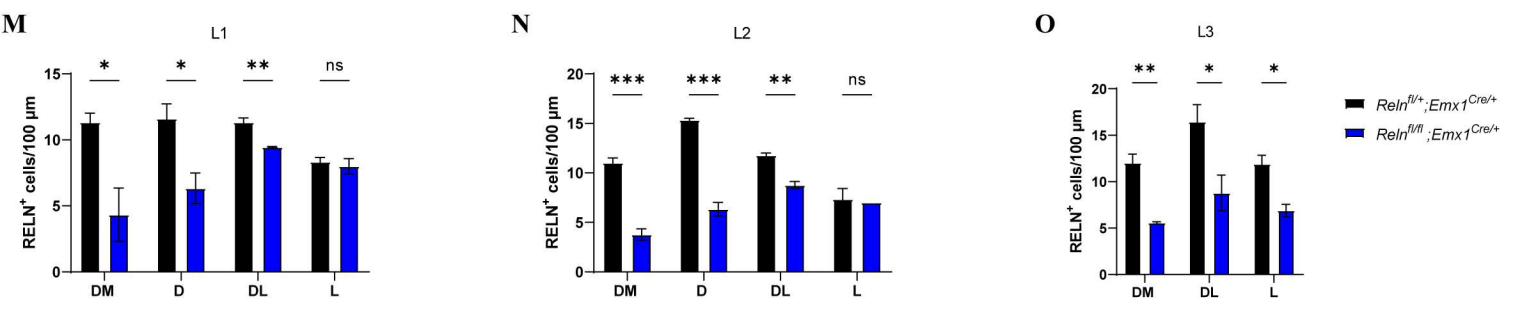
Yoshida, M., Assimacopoulos, S., Jones, K. R., & Grove, E. A. (2006). Massive loss of Cajal-Retzius cells does not disrupt neocortical layer order. *Development*, *133*(3), 537–545. https://doi.org/10.1242/dev.02209

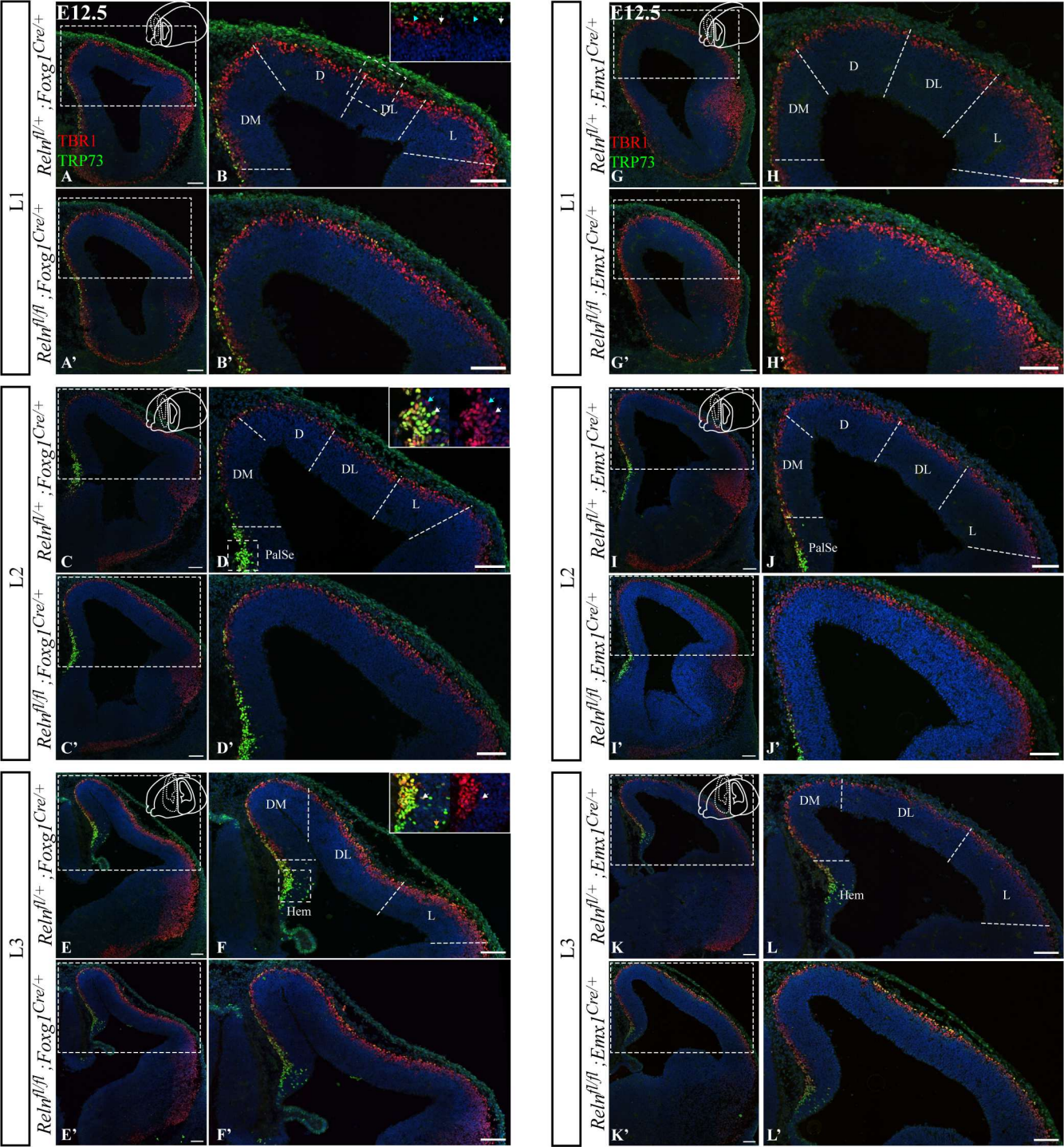
Yoshinaga, S., Honda, T., Kubo, K.-I., & Nakajima, K. (2022). Dab1-deficient deep layer neurons prevent Dab1-deficient superficial layer neurons from entering the cortical plate. *Neuroscience Research*, *180*, 23–35. https://doi.org/10.1016/j.neures.2022.03.011

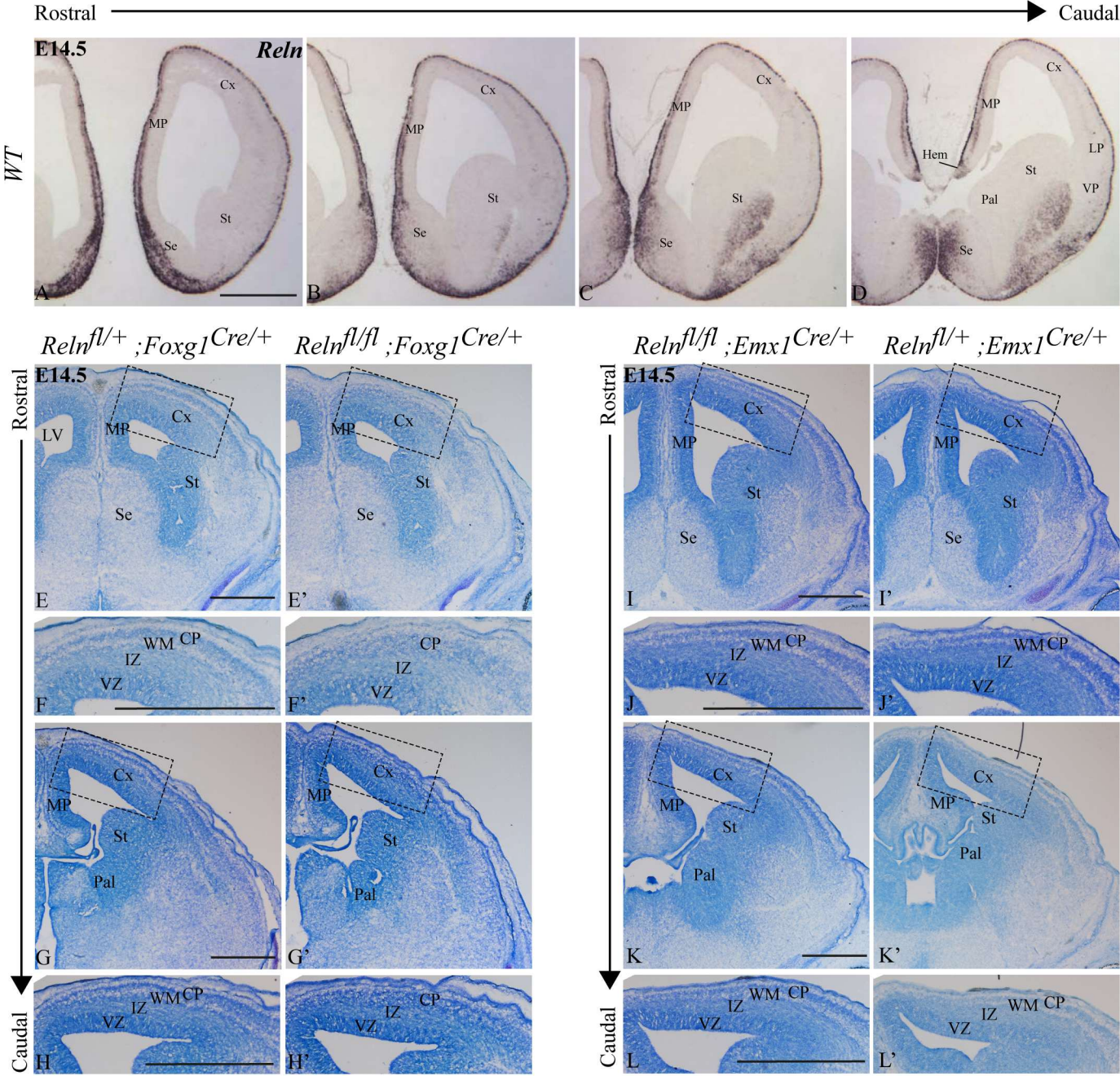
Zhao, S., Chai, X., Förster, E., & Frotscher, M. (2004). *Reelin is a positional signal for the lamination of dentate granule cells*. 5117–5125. https://doi.org/10.1242/dev.01387

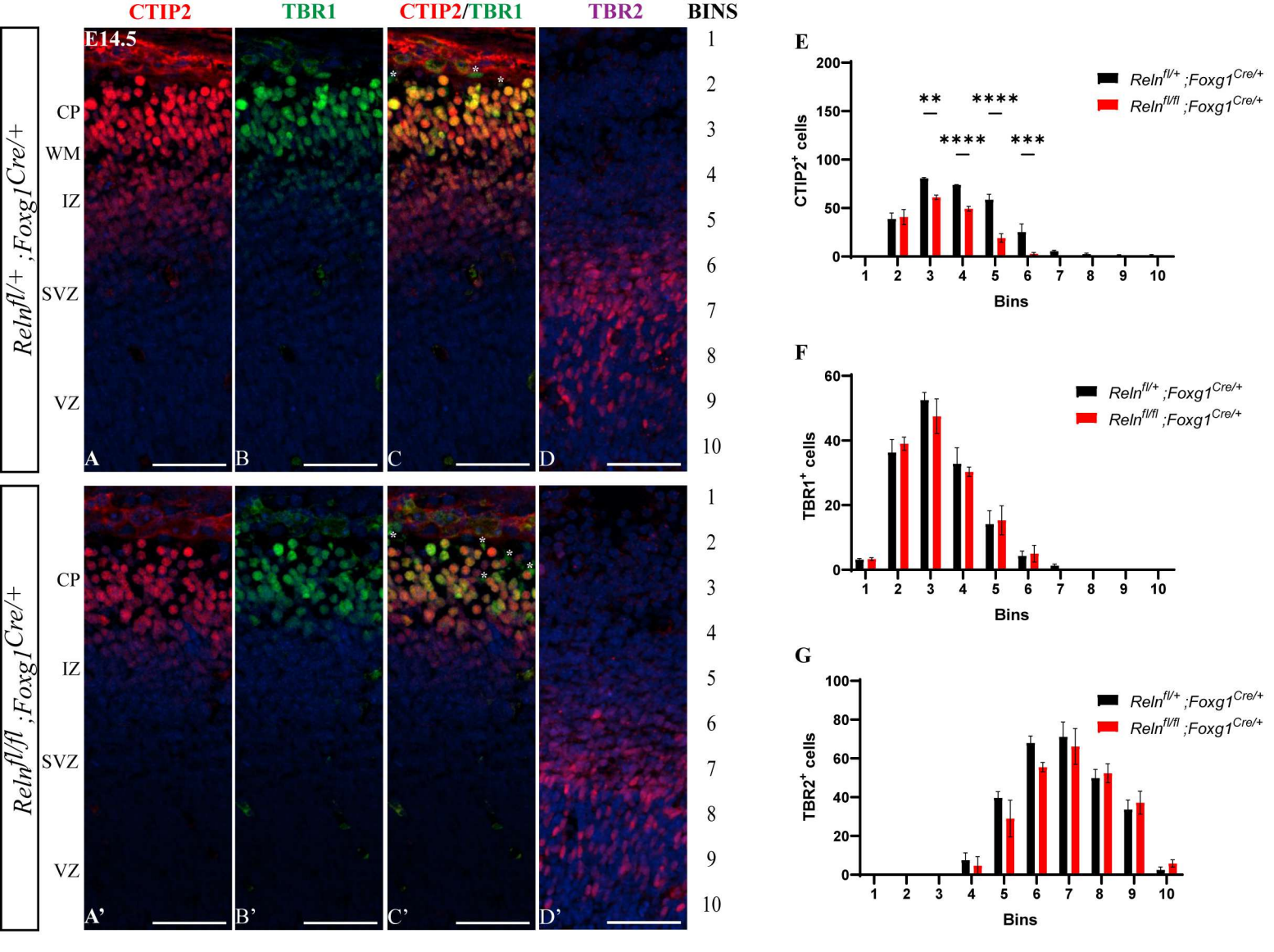

A
Reln
1
2
3
4
5
7
11
37-38
65
loxP sites
RELN antibody
Reln probe
E12.5
Cx
St
Se
B Reln
C
Reln fl/+ ;Foxg1Cre/+
B'
C'
Reln fl/fl ;Foxg1Cre/+
F
RELN
HOECHST
G
F'
G'
D Reln
E
Reln fl/+ ;Emx1Cre/+
D'
E'
Reln fl/fl ;Emx1Cre/+
H
I
H'
I'

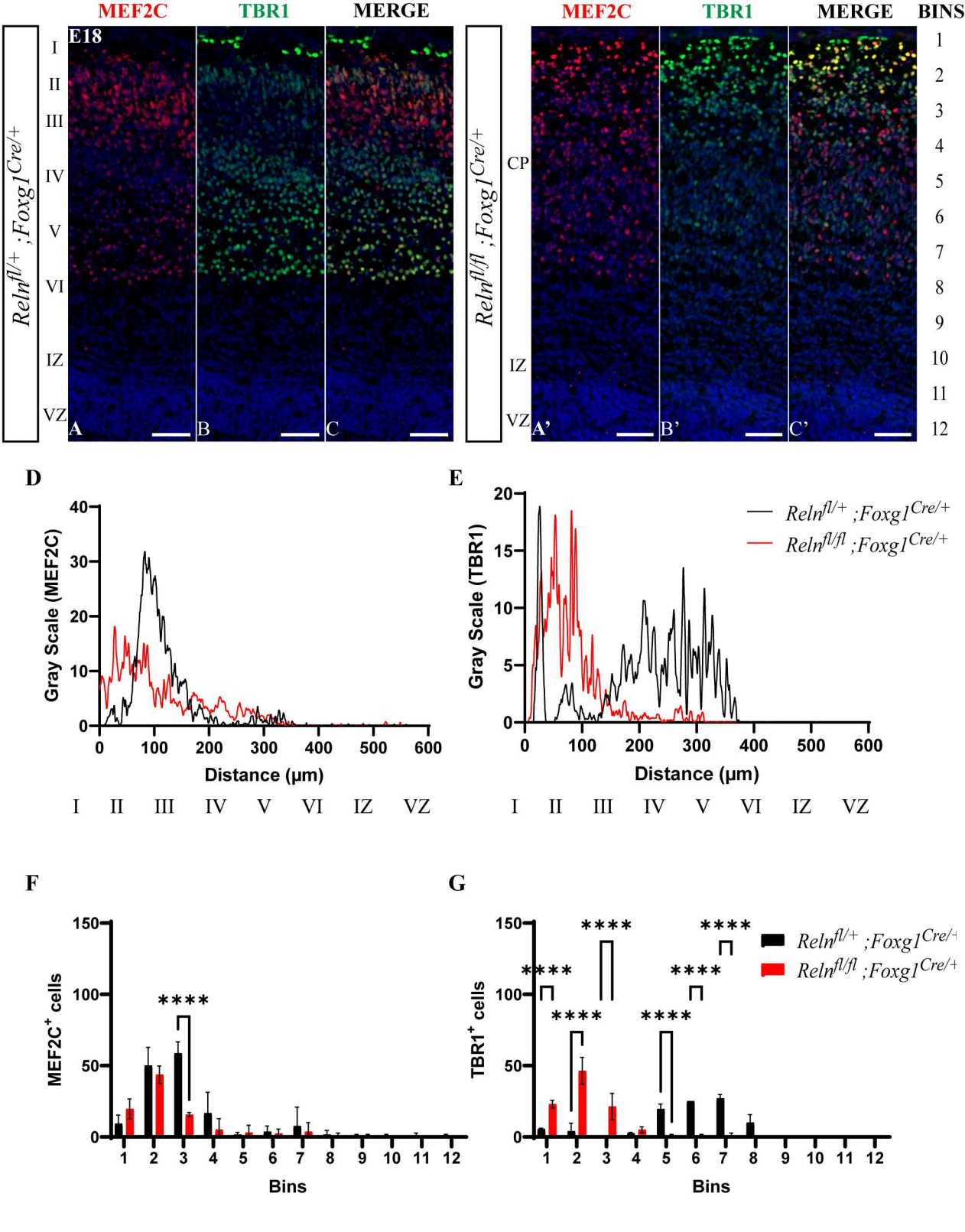

E12.5
TBR1
RELN
D
DM
DL
L
A
B
A'
B'
G
H
G'
H'
C
D
C'
D'
I
J
I'
J'
E
F
E'
F'
K
L
K'
L'
L1
L2
L3
Reln^fl/+ ;Foxg1^Cre/+
Reln^fl/fl ;Foxg1^Cre/+
Reln^fl/+ ;Emx1^Cre/+
Reln^fl/fl ;Emx1^Cre/+

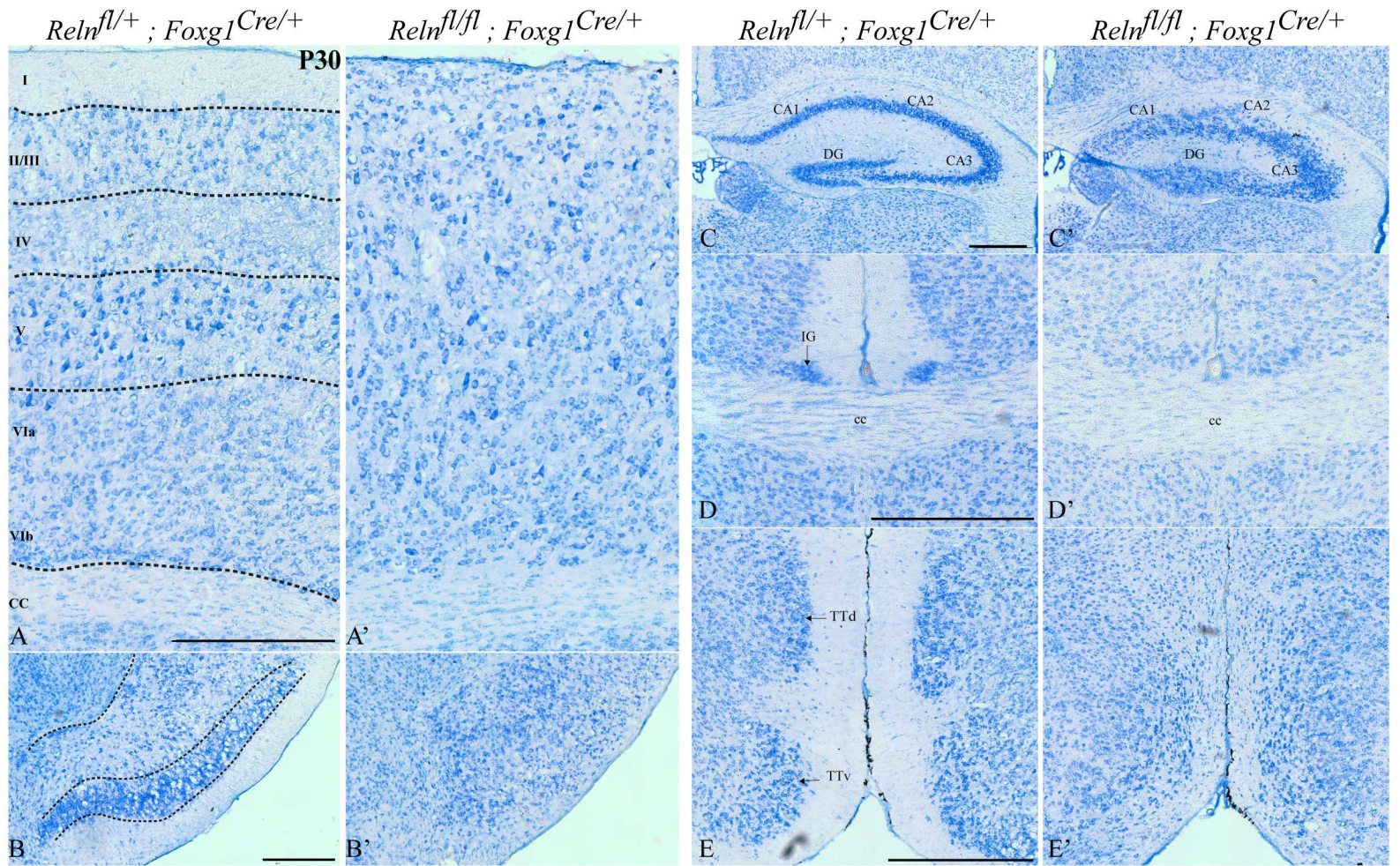

M
L1
N
L2
O
L3
RELN+ cells/100 µm
DM
D
DL
L
ns
Reln^fl/+ ;Emx1^Cre/+
Reln^fl/fl ;Emx1^Cre/+

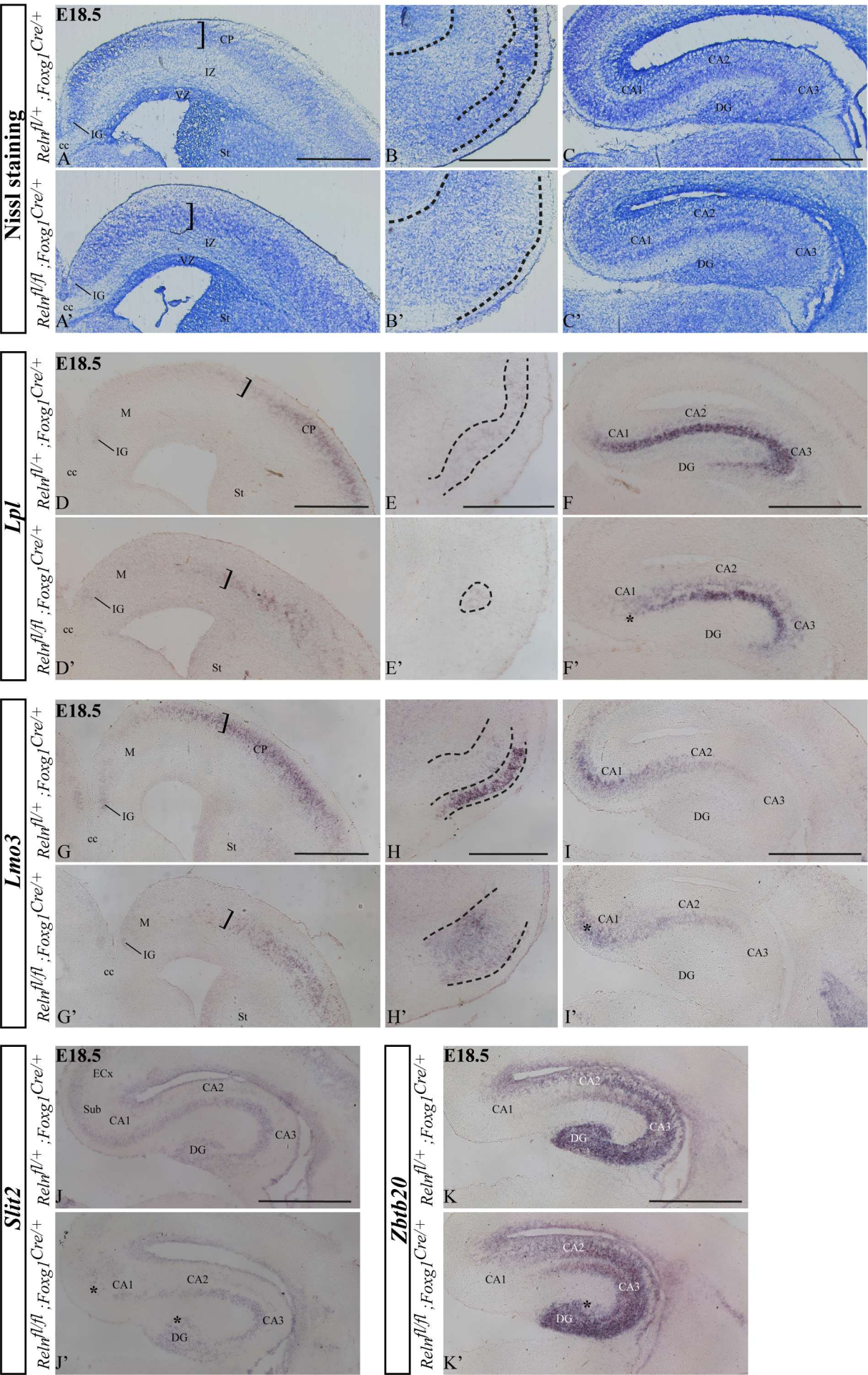

E12.5
TBR1
TRP73
D
DM
DL
L
PalSe
Hem
L1
L2
L3
Reln fl/+ ;Foxg1 Cre/+
Reln fl/fl ;Foxg1 Cre/+
Reln fl/+ ;Emx1 Cre/+
Reln fl/fl ;Emx1 Cre/+
A
A'
B
B'
C
C'
D
D'
E
E'
F
F'
G
G'
H
H'
I
I'
J
J'
K
K'
L
L'

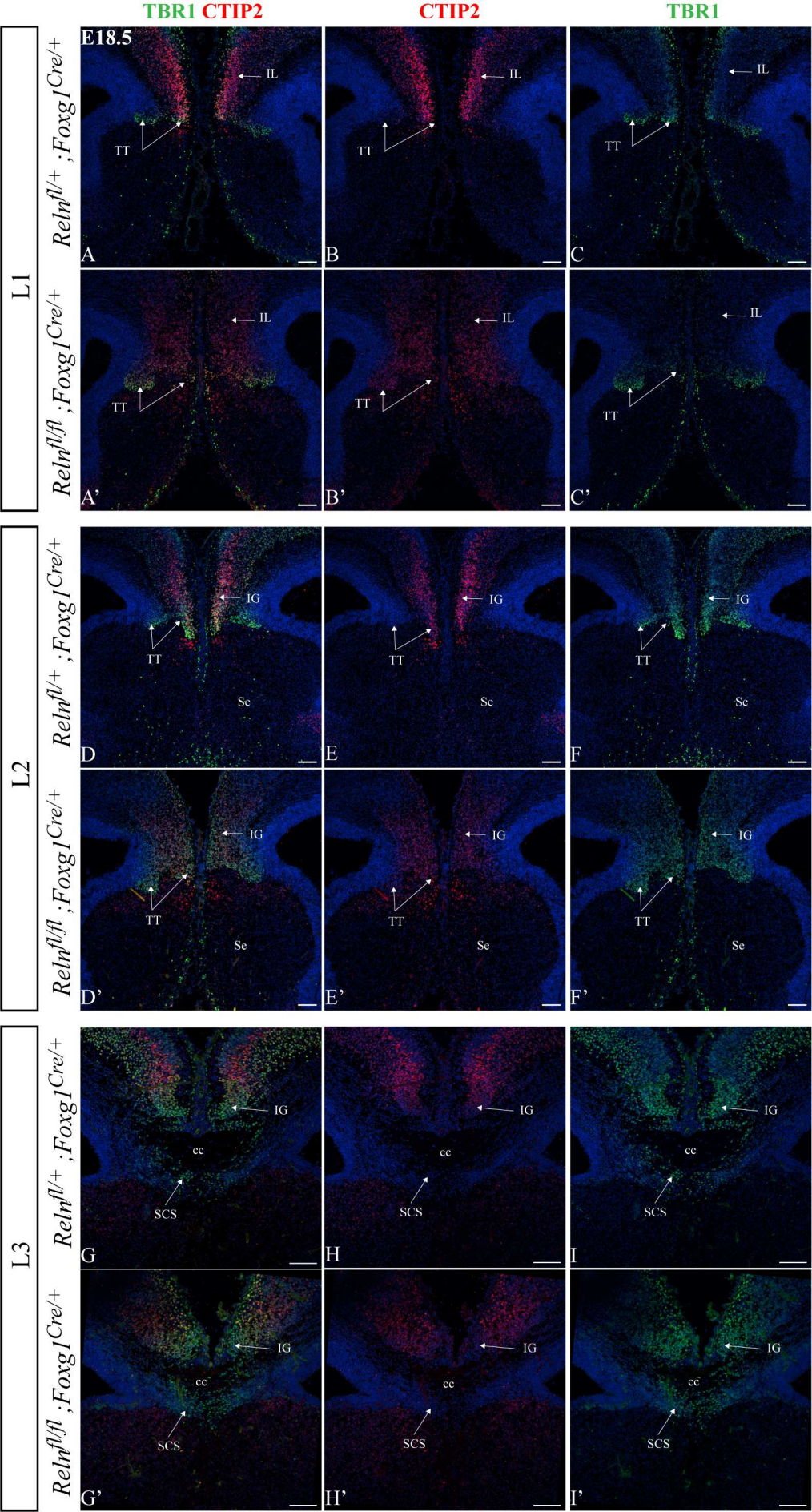

Rostral
Caudal
WT
E14.5
Reln
Cx
MP
St
Se
A
B
C
D
Hem
LP
VP
Pal
Reln fl/+ ;Foxg1 Cre/+
Reln fl/fl ;Foxg1 Cre/+
Reln fl/fl ;Emx1 Cre/+
Reln fl/+ ;Emx1 Cre/+
LV
WM
CP
IZ
VZ
E
E'
F
F'
G
G'
H
H'
I
I'
J
J'
K
K'
L
L'

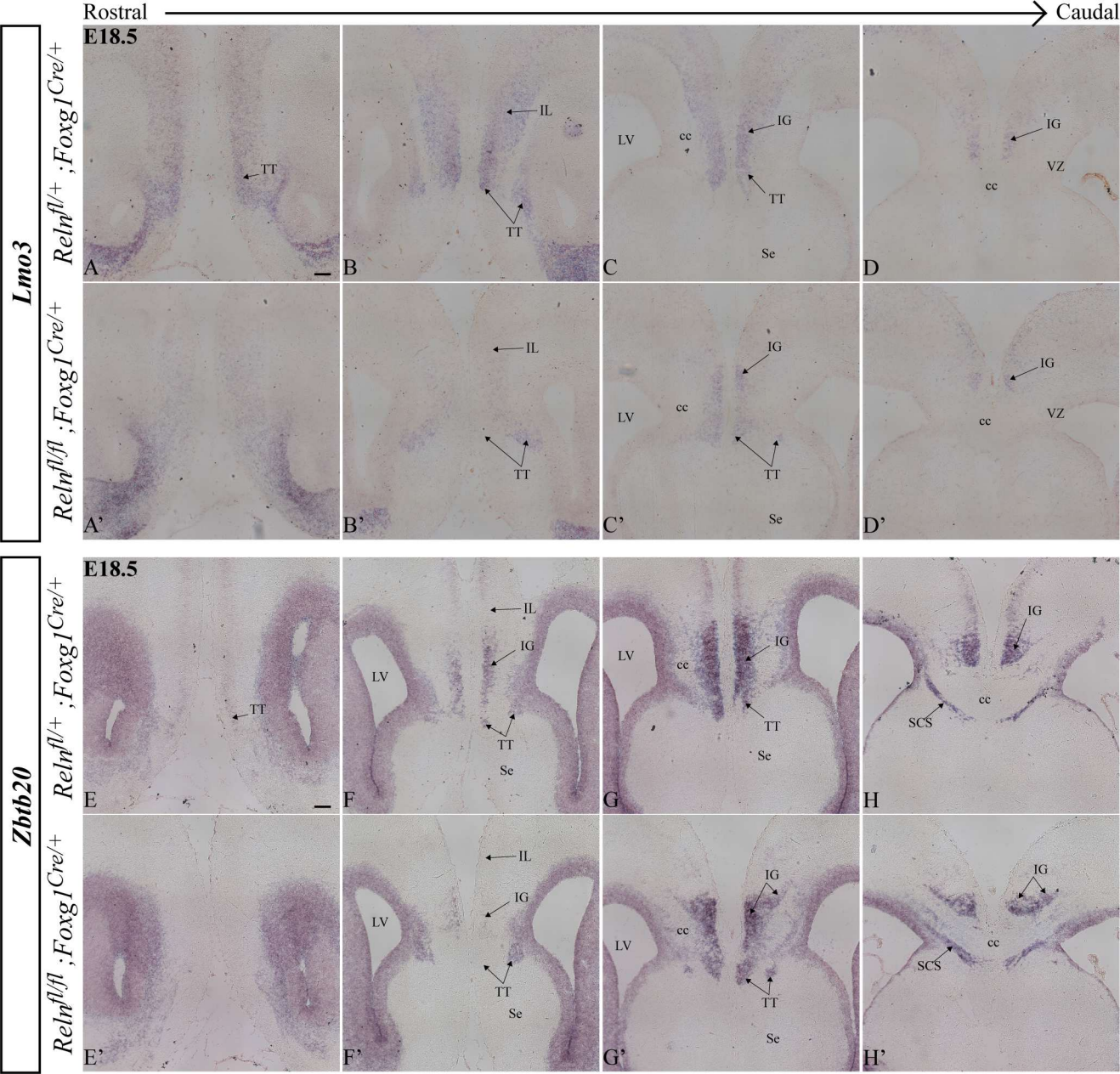

CTIP2
TBR1
CTIP2/TBR1
TBR2
BINS
E14.5
Reln fl/+ ;Foxg1 Cre/+
Reln fl/fl ;Foxg1 Cre/+
CP
WM
IZ
SVZ
VZ
A
B
C
D
A'
B'
C'
D'
1
2
3
4
5
6
7
8
9
10
E
CTIP2+ cells
Bins
**
****
****
***
F
TBR1+ cells
G
TBR2+ cells

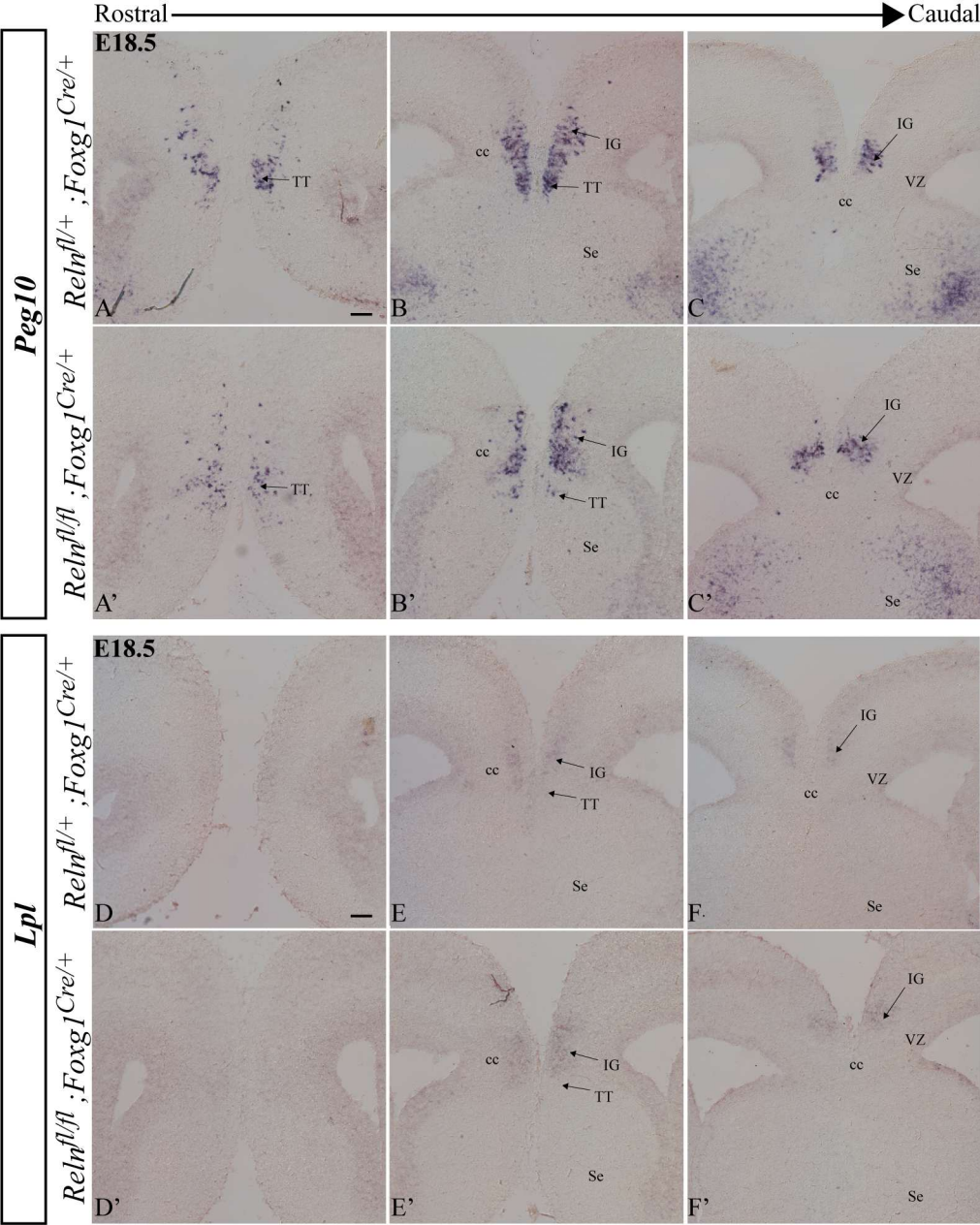

MEF2C
TBR1
MERGE
BINS
E18
Reln^fl/+ ;Foxg1^Cre/+
Reln^fl/fl ;Foxg1^Cre/+
I
II
III
IV
V
VI
IZ
VZ
CP
A
B
C
A'
B'
C'
1
2
3
4
5
6
7
8
9
10
11
12
D
Gray Scale (MEF2C)
Distance (μm)
E
Gray Scale (TBR1)
F
MEF2C+ cells
Bins
G
TBR1+ cells
****

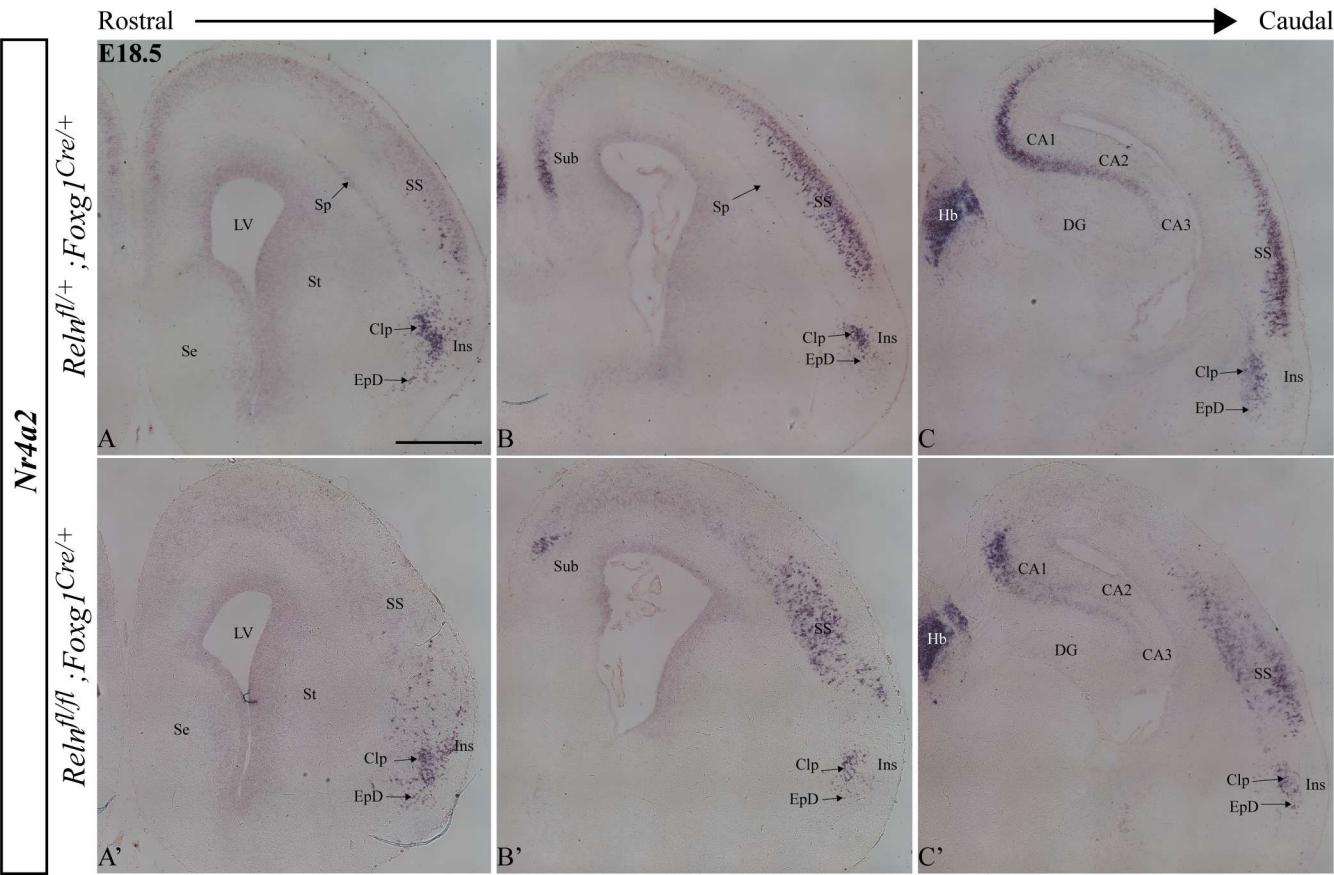

Reln fl/+ ; Foxg1 Cre/+
Reln fl/fl ; Foxg1 Cre/+
Reln fl/+ ; Foxg1 Cre/+
Reln fl/fl ; Foxg1 Cre/+
P30
I
II/III
IV
V
VIa
VIb
CC
A
A'
B
B'
CA1
CA2
DG
CA3
C
C'
IG
cc
D
D'
TTd
TTv
E
E'


Nissl staining
E18.5
Reln fl/+ ;Foxg1 Cre/+
Reln fl/fl ;Foxg1 Cre/+
CP
IZ
VZ
IG
cc
St
CA1
CA2
CA3
DG
A
A'
B
B'
C
C'
Lpl
M
D
D'
E
E'
F
F'
*
Lmo3
G
G'
H
H'
I
I'
Slit2
ECx
Sub
J
J'
Zbtb20
K
K'


TBR1 CTIP2
CTIP2
TBR1
E18.5
L1
L2
L3
Reln^fl/+ ;Foxg1^Cre/+
Reln^fl/fl ;Foxg1^Cre/+
IL
TT
IG
Se
cc
SCS
A
B
C
A'
B'
C'
D
E
F
D'
E'
F'
G
H
I
G'
H'
I'


Rostral
Caudal
Lmo3
Zbtb20
E18.5
Reln^fl/+ ;Foxg1^Cre/+
Reln^fl/fl ;Foxg1^Cre/+
A
B
C
D
A'
B'
C'
D'
E
F
G
H
E'
F'
G'
H'
TT
IL
IG
LV
cc
Se
VZ
SCS


Rostral
Caudal
Peg10
Lpl
E18.5
Reln fl/+ ;Foxg1 Cre/+
Reln fl/fl ;Foxg1 Cre/+
A
B
C
A'
B'
C'
D
E
F
D'
E'
F'
TT
IG
cc
VZ
Se


Rostral
Caudal
Nr4a2
E18.5
Reln^fl/+ ;Foxg1^Cre/+
Reln^fl/fl ;Foxg1^Cre/+
LV
Sp
SS
St
Se
Clp
Ins
EpD
A
Sub
B
CA1
CA2
Hb
DG
CA3
C
A'
B'
C'

Supplementary Files

This is a list of supplementary files associated with this preprint. Click to download.

- Supplementaryfigures.pdf